AGU PUBLICATIONS

Water Resources Research

RESEARCH ARTICLE
10.1002/2016WR020126

**Key Points:**
- Cold, dry, and wind-exposed conditions increase the magnitude of negative latent heat fluxes at high-elevation sites of the semiarid Andes
- Melt dominates at low-elevation, low-albedo sites, but sublimation prevails at wind-exposed, strong irradiated, high-elevation sites
- The performance of an enhanced temperature-index model decreases as sublimation-favorable conditions dominate

**Supporting Information:**
- Supporting Information S1

**Correspondence to:**
A. Ayala,
ayala@ifu.baug.ethz.ch

**Citation:**
Ayala, A., F. Pellicciotti, S. MacDonell, J. McPhee, and P. Burlando (2017), Patterns of glacier ablation across North-Central Chile: Identifying the limits of empirical melt models under sublimation-favorable conditions, *Water Resour. Res.*, *53*, 5601–5625, doi:10.1002/2016WR020126.

Received 15 NOV 2016
Accepted 8 JUN 2017
Accepted article online 14 JUN 2017
Published online 10 JUL 2017

© 2017. American Geophysical Union. All Rights Reserved.

# Patterns of glacier ablation across North-Central Chile: Identifying the limits of empirical melt models under sublimation-favorable conditions

**A. Ayala[1], F. Pellicciotti[1,2], S. MacDonell[3], J. McPhee[4,5], and P. Burlando[1]**

[1]Institute of Environmental Engineering, Department of Civil, Environmental and Geomatic Engineering, ETH-Zurich, Zurich, Switzerland, [2]Department of Geography, Faculty of Engineering and Environment, Northumbria University, Newcastle, UK, [3]Centro de Estudios Avanzados en Zonas Áridas (CEAZA), La Serena, Chile, [4]Department of Civil Engineering, Faculty of Physical and Mathematical Sciences, Universidad de Chile, Santiago, Chile, [5]Advanced Mining Technology Centre (AMTC), Faculty of Physical and Mathematical Sciences, Universidad de Chile, Santiago, Chile

**Abstract** We investigate the energy balance and ablation regimes of glaciers in high-elevation, dry environments using glaciometeorological data collected on six glaciers in the semiarid Andes of North-Central Chile (29–34°S, 3127–5324 m). We use a point-scale physically based energy balance (EB) model and an enhanced Temperature-Index (ETI) model that calculates melt rates only as a function of air temperature and net shortwave radiation. At all sites, the largest energy inputs are net shortwave and incoming longwave radiation, which are controlled by surface albedo and elevation, respectively. Turbulent fluxes cancel each other out at the lower sites, but as elevation increases, cold, dry and wind-exposed conditions increase the magnitude of negative latent heat fluxes, associated with large surface sublimation rates. In midsummer (January), ablation rates vary from 67.9 mm w.e. $d^{-1}$ at the lowest site (∼100% corresponding to melt), to 2.3 mm w.e. $d^{-1}$ at the highest site (>85% corresponding to surface sublimation). At low-elevation, low-albedo, melt-dominated sites, the ETI model correctly reproduces melt using a large range of possible parameters, but both the performance and parameter transferability decrease with elevation for two main reasons: (i) the air temperature threshold approach for melt onset does not capture the diurnal variability of melt in cold and strong irradiated environments and (ii) energy losses decrease the correlation between melt and net shortwave radiation. We summarize our results by means of an elevation profile of ablation components that can be used as reference in future studies of glacier ablation in the semiarid Andes.

## 1. Introduction

In semiarid high-elevation regions, seasonal snow provides the largest contribution to freshwater resources during normal and wet years [*Barnett et al.*, 2005; *Masiokas et al.*, 2006; *Favier et al.*, 2009], but glacier melt ensures minimum flow conditions during the end-of-summer and drought periods [*Kaser et al.*, 2010; *Ragettli and Pellicciotti*, 2012; *Ragettli et al.*, 2016]. In semiarid North-Central Chile (29°–34°S), fresh water resources originating in the Andes Cordillera are used for human consumption, agriculture, industry, energy generation, and mining. During the last decade, increased demand for water resources [*Meza*, 2013] and a severe drought [*Boisier et al.*, 2016; *Cornwell et al.*, 2016] have led to a situation of extreme water stress from which social and economic conflicts have arisen [*Urkidi*, 2010; *Oyarzún and Oyarzún*, 2011]. In this context, there is a need for a better understanding of cryospheric and hydrological processes in the Andes and a more accurate quantification of the water resources provided by glaciers and seasonal snow cover [*Ohlanders et al.*, 2013; *Pellicciotti et al.*, 2014; *Ayala et al.*, 2016; *Ragettli et al.*, 2016]. In this study, we focus on the understanding of the glacier energy balance and ablation across this dry, high-elevation environment and on the implications for meltwater generation and its modeling.

Melt from snow and ice can be calculated (i) as a residual of the physically based equations that describe the energy balance at the glacier-atmosphere interface, or (ii) as the result of simplified formulae that characterize the energy balance equations with a small number of input variables (usually air temperature) and empirical factors. The main disadvantages of energy balance models are the large uncertainties in the estimation of meteorological and surface input variables and physical parameters at the distributed scale and

at remote high-elevation sites [*MacDougall and Flowers*, 2011; *Gabbi et al*., 2014; *Pellicciotti et al*., 2014]. On the other hand, temperature-index models can be limited by the sometimes excessive simplification of the physical processes and the transferability in space and time of their empirical factors [*Heynen et al*., 2013; *Kumar et al*., 2013; *Gabbi et al*., 2014; *Wheler et al*., 2014]. Temperature-index models have been mostly calibrated during midsummer conditions at relatively low elevations, where the snow or ice surface is close to its melting point [*Braithwaite*, 1995; *Ohmura*, 2001; *Pellicciotti et al*., 2008; *Carenzo et al*., 2009]. With few exceptions, the overall performance of empirical melt models in dry environments under conditions favorable to sublimation has rarely been assessed [*Ebnet et al*., 2005; *Sicart et al*., 2008]. These studies analyzed the energy balance of glaciers in diverse environments and observed that negative latent heat fluxes associated with surface sublimation can considerably reduce the energy available for melt [*Hock*, 2003; *Ebnet et al*., 2005] and, thus, might reduce the correlation between melt and air temperature [*Sicart et al*., 2008], potentially decreasing the performance of temperature-index models. However, to date, the magnitude of this decrease in performance has not been clearly quantified.

Sublimation can occur at the surface or during aeolian transportation, known as blowing snow sublimation. While surface sublimation can be obtained from the calculation of the turbulent latent heat fluxes at the glacier-atmosphere interface, the estimation of blowing snow sublimation requires an additional set of equations, which describe the dynamics of saltation and suspension layers and the sublimation rates of snow particles in the air [*Pomeroy et al*., 1993; *Liston and Sturm*, 1998; *Lehning et al*., 2006]. Sublimation is often neglected in glaciohydrological models due to its relatively low magnitude in comparison to melt, large uncertainties associated with the calculation of surface-atmosphere turbulent exchanges and a general lack of high-elevation meteorological input data for its calculation [*Lutz et al*., 2014; *Ragettli et al*., 2015; *Shea et al*., 2015]. Sublimation is highly variable in space and time and can be large at sites where wind-induced snow transport is frequent and efficient [*Strasser et al*., 2008; *MacDonald et al*., 2010; *Groot Zwaaftink et al*., 2013] and at sites with low air humidity, high incoming shortwave radiation and strong winds, such as the semiarid Andes [*Favier et al*., 2009; *Gascoin et al*., 2013].

Previous studies have found that sublimation is an important process in North-Central Chile. In the Pascua Lama catchment (29°S), *Gascoin et al*. [2013] estimated that sublimation represents about 71–73% of total ablation during a complete snow season, with sublimation from blowing snow accounting up to 18% of total ablation. Using an ice core from Tapado Glacier in northern Chile (30.1°S), *Ginot et al*. [2006] concluded that 60% of annual accumulation at 5536 m above sea level (asl) was lost as surface sublimation during the period 1962–1999. At the point scale, other authors have quantified surface sublimation with different results depending on elevation, latitude, and local climate [*Corripio et al*., 2008; *Pellicciotti et al*., 2008; *MacDonell et al*., 2013]. A particularly interesting surface feature that is connected to surface sublimation are snow or ice penitentes. Penitentes have been reported at several high-elevation sites of the semiarid Andes and are an indication of melt and surface sublimation occurring at the same time, with sublimation taking place at the top of the cones and melt at the bottom [*Lliboutry*, 1954; *Corripio and Purves*, 2005; *Sinclair and MacDonell*, 2015]. Penitentes are able to modify the surface energy balance by reducing the overall surface albedo [*Lhermitte et al*., 2014] and increasing the aerodynamic surface roughness length [*Corripio and Purves*, 2005; *Nicholson et al*., 2016]. Despite these important advances, there has not been yet any attempt to quantify turbulent latent heat fluxes and surface sublimation on several glaciers in a single comparative study, with most studies focusing on energy balance processes and measurements at one site only [*Corripio and Purves*, 2005; *Ginot et al*., 2006; *Pellicciotti et al*., 2008; *Gascoin et al*., 2011; *MacDonell et al*., 2013], or inferring surface sublimation amounts from regional climate models [*Favier et al*., 2009].

Using a unique multisite glaciometeorological data set collected on six glaciers in the semiarid Andes of North-Central Chile (29–34°S), we aim to: (i) describe and quantify the summer glacier energy balance and ablation over a large gradient of elevation and latitude and (ii) establish a link between the characteristics of the glacier energy balance and the performance and parameter transferability of a temperature-index model. As an example of a temperature-index model, we use the Enhanced Temperature-Index (ETI) model developed by *Pellicciotti et al*. [2005], which has been previously used in the region [*Pellicciotti et al*., 2008; *Ragettli and Pellicciotti*, 2012; *Ayala et al*., 2016].

## 2. Study Sites and Data

### 2.1. Study Region and Selected Glaciers

In semiarid North-Central Chile (29°–34°S), the Andes Cordillera has a width of approximately 100 km and reaches an elevation of 6961 m asl. The climate varies from extremely dry to the north of the study region, close to the Atacama Desert, to Mediterranean in Central Chile [*Garreaud*, 2009]. Precipitation predominantly occurs during winter [*Falvey and Garreaud*, 2007] and is controlled by El Niño Southern Oscillation (ENSO) and the seasonal north-south displacement of the South Pacific Anticyclone [*Grimm et al*., 2000; *Montecinos and Aceituno*, 2003]. In general, high annual amounts of precipitation are associated with El Niño events and low amounts are associated with La Niña events, defining a strong interannual variability [*Masiokas et al*., 2006; *Falvey and Garreaud*, 2007]. Austral summer is dominated by extremely dry and stable atmospheric conditions with little cloudiness that result in the surface energy balance being dominated by intense shortwave radiation [*Lliboutry*, 1954; *Corripio et al*., 2008; *Pellicciotti et al*., 2008]. As a result of these conditions, precipitation and air temperature have a strong seasonality [*Carrasco et al*., 2005; *Falvey and Garreaud*, 2007; *Valdés-Pineda et al*., 2015]. In this study, we define as ablation season the period starting at the time of maximum snow accumulation (August–September) and ending at the beginning of the next winter precipitation events (April–May).

Debris-free glaciers to the north of 30°S are located above 5000 m asl, have small surface areas, show few surface signs of flow and are usually difficult to distinguish from patches of permanent snow accumulation [*Nicholson et al*., 2010]. Further south, the transition from a dry to a Mediterranean climate with larger values of annual precipitation is reflected in the presence of valley glaciers that reach elevations below 4000 m asl [*Casassa*, 1995; *Bown et al*., 2008]. Our study sites can be grouped in two clusters, which we refer to as the North Chile and Central Chile clusters (Figure 1 and Table 1). The North-Chile cluster is located between 29 and 30°S and includes Guanaco and Tapado glaciers, whereas the Central Chile cluster is located between 32 and 34°S and includes Juncal Norte, Bello, Yeso, and San Francisco glaciers. The relation between latitude and mean glacier elevation in the semiarid Andes can be observed in Figure 1b. As most of our analyses are based on elevation differences, we provide a description of each glacier in an order of increasing elevation of the study sites (described in section 2.2).

Juncal Norte Glacier is located in the Aconcagua River catchment, it is one of the few north-facing glaciers of the region and flows from the upper cirque along a narrow valley (approximately 700 m wide) surrounded by steep valley walls (Figure 1a, box C). Juncal Norte Glacier is one of the most studied glaciers of the region. Previous studies include the description and/or modeling of its energy balance [*Corripio and Purves*, 2005; *Pellicciotti et al*., 2008], air temperature distribution [*Petersen and Pellicciotti*, 2011; *Ayala et al*., 2015], geomorphology [*Janke et al*., 2015], and hydrology [*Ragettli and Pellicciotti*, 2012; *Ohlanders et al*., 2013; *Ragettli et al*., 2016]. San Francisco Glacier is located in El Morado National Park within the Maipo River catchment. It is a relatively small hanging glacier and its fragmented shape suggests that it is a remnant of a larger system (Figure 1a, box E). The glacier has a south-facing aspect and is protected from the dominant northerly winds. Bello and Yeso glaciers are two south-facing neighbor glaciers located 70 km east from the city of Santiago in the Maipo River catchment (Figure 1a, box D). They provide a key hydrological contribution to one of the main drinking-water reservoirs of Santiago (El Yeso reservoir) [*Ayala et al*., 2016].

Tapado Glacier is the largest glacier in the upper Elqui River catchment (Figure 1a, box B). It is an isolated ice mass surrounded by higher, ice-free peaks, which suggests that specific conditions, such as snow redistribution and solar radiation shading, must be met to explain the presence of the glacier [*Ginot et al*., 2006; *Lhermitte et al*., 2014]. Low sections of the glacier are covered by debris or have evolved into a rock glacier [*Azócar and Brenning*, 2010; *Janke et al*., 2015]. Guanaco Glacier lies at the Chile-Argentina international border within the Huasco River catchment (Figure 1a, box A). It is one the largest glaciers in this area, but it has a relatively small surface area (1.8 $km^2$). Guanaco Glacier has a south-facing aspect that suggests that shading from solar radiation and shelter from predominant northwesterly winds was important to explain its formation in this extremely arid region [*Nicholson et al*., 2010; *Rabatel et al*., 2011; *Gascoin et al*., 2013]. The upper section of the glacier is exposed to intense winds which control its energy and mass balance by causing large negative latent heat fluxes and sublimation [*MacDonell et al*., 2013].

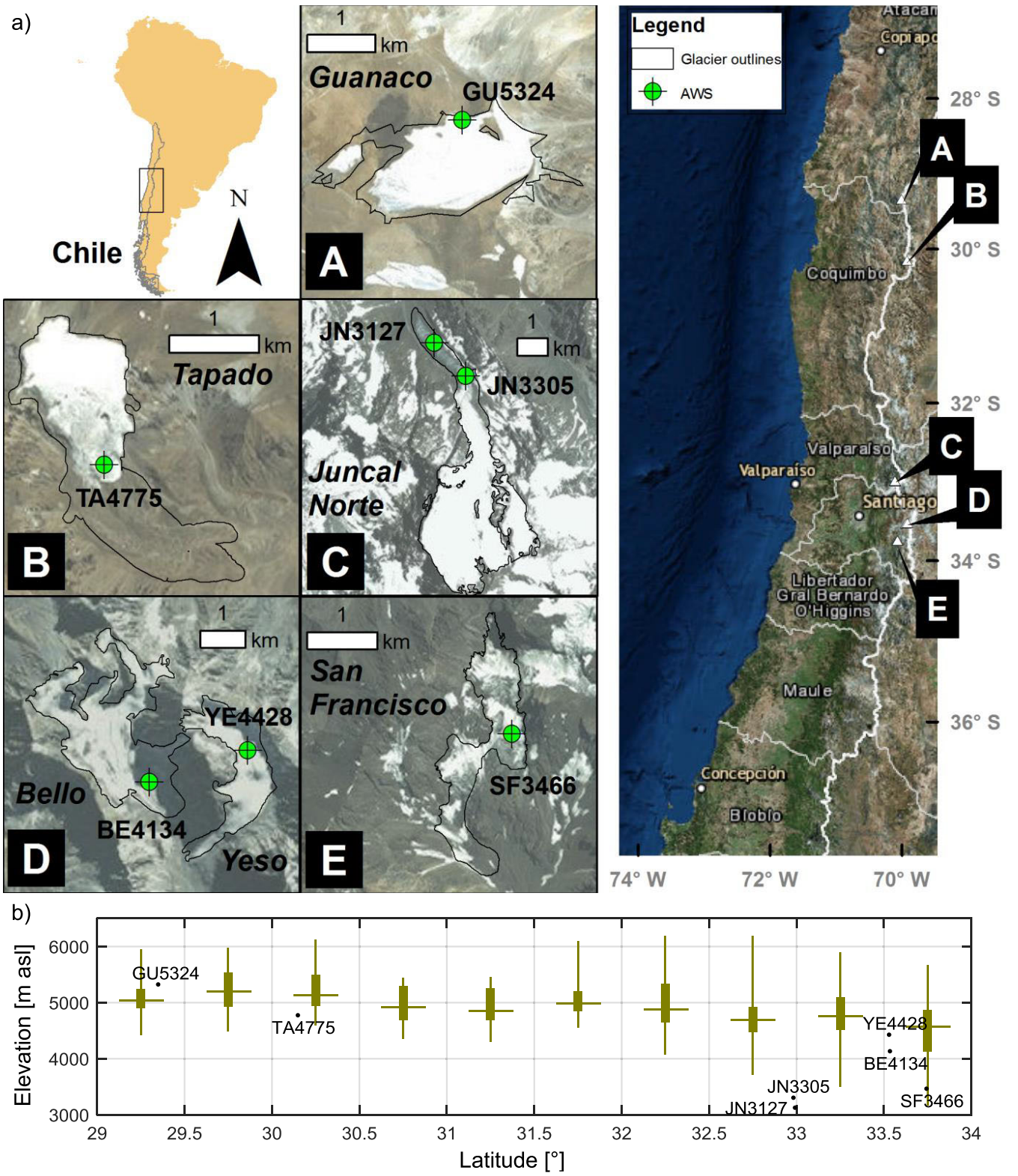


**Figure 1.** (a) Location of Guanaco (A), Tapado (B), Juncal Norte (C), Bello and Yeso (D), and San Francisco (E) glaciers in North-Central Chile (29°S–34°S). AWSs on each glacier are shown with their elevation as suffix. Glaciers outlines were extracted from the Chilean National Inventory [*DGA*, 2010]. (b) Location of the AWSs in the latitudinal distribution of the mean elevation of Andean glaciers [*Arendt et al*., 2014] between 29°S and 34°S. The central mark of each boxplot is the median, the box shows the 25th and 75th percentiles and the whiskers extend to the most extreme data points.

**Table 1.** Main Characteristics of Glaciers, AWSs, and Instruments Used in This Study[a]

| Glacier | Elevation Range (m asl) | ELA (m asl) | Area ($km^2$) | Station Name | Station Location | Period of Measurements Time Resolution, Sampling Rates, and Instrumental Height | Instruments |
|---|---|---|---|---|---|---|---|
| Juncal Norte | 2900<br>5910 | 4500<br>[*Ragettli et al.*, 2014] | 7.6 | JN3127 | 3127 m asl<br>32.991S<br>70.109W | 07–12-2008 to 15–02-2009<br>1 h, 5s<br>2.0 m | SR: Kipp & Zonen CM7B<br>Ta & RH: Rotronic MP-103A (aspirated)<br>WS: Young S-WMON |
| | | | | JN3305 | 3305 m asl<br>32.982S<br>70.114W | 08–12-2008 to 05–02-2009<br>1 h, 5s<br>2.0 m | SH: Campbell SR50<br>Datalogger: Campbell CR10X |
| San Francisco | 2670<br>4020 | | 1.8 | SF3466 | 3466 m asl<br>33.743S<br>70.074W | 05–11-2013 to 24–01-2014<br>10 min, 10s<br>2.0 m<br>05–11-2014 to 08–04-2015<br>10 min, 10s<br>2.0 m | Ta, RH: Young 41382 (aspirated)<br>SR & LR: Kipp & Zonen CNR4<br>SH: Campbell SR50<br>WS: Young 05103<br>Datalogger: Campbell CR3000 |
| Bello | 3870<br>5000 | 4600<br>[*Ayala et al.*, 2016] | 4.8 | BE4134 | 4134 m asl<br>33.534S<br>69.940W | 15–11-2013 to 19–03-2014<br>1 h, 10s<br>2.3 m<br>22–10-2014 to 19–03-2015<br>1 h, 10s<br>2.3 m | |
| Yeso | 3750<br>5145 | 4650<br>[*Ayala et al.*, 2016] | 3.1 | YE4428 | 4428 m asl<br>33.529S<br>69.920W | 15–11-2013 to 19–03-2014<br>1 h, 10s<br>2.0 m<br>05–11-2014 to 19–01-2015<br>1 h, 10s<br>2.0 m | |
| Tapado | 4100<br>5520 | 5300<br>[*Ginot et al.*, 2006] | 2.2 | TA4775 | 4775 m asl<br>30.148S<br>69.925W | 23–11-2013 to 10–01-2014<br>10 min, 10s<br>2.2 m | |
| Guanaco | 4990<br>5350 | | 1.8 | GU5324 | 5324 m asl<br>29.349S<br>70.018W | 01–11-2008 to 30–04-2011<br>1 h, 10s<br>4.2 m (initial), 5.7 m (final) | Ta, RH: Vaisala HMO45C (not aspirated)<br>WS: Young 05103<br>SR & LR: Kipp & Zonen CNR1<br>SH: Campbell SR50<br>Datalogger: CR1000 |

[a]Ta: air temperature, RH: relative humidity, WS: wind speed, SR: shortwave radiation, LR: longwave radiation, SH: surface height.

### 2.2. Meteorological and Glaciological Measurements

We installed a set of AWSs on San Francisco, Bello, Yeso, and Tapado glaciers for the duration of the ablation seasons 2013–2014 and 2014–2015 (Figure 1 and Table 1). We added to these measurements two previously recorded data sets on Juncal Norte and Guanaco glaciers. Data on Juncal Norte Glacier were measured at two AWSs during the ablation season 2008–2009 [*Petersen and Pellicciotti*, 2011; *Ragettli and Pellicciotti*, 2012] and data on Guanaco Glacier were recorded at an AWS that measured during a 2.5 years period from November 2008 to April 2011 [*MacDonell et al.*, 2013]. Based on previous estimations of the Equilibrium Line Altitude (ELA) (Table 1), the AWSs were placed on the glacier ablation area. With the exception of the AWS on Guanaco Glacier, AWSs were allowed to sink together with the melting surface. In this way, the height of the sensors remained constant throughout the study periods. The AWS at Guanaco Glacier was drilled into the ice and thus fixed to the glacier surface. Consequently, as the glacier surface ablated, the sensor height increased.

The AWSs recorded air temperature, relative humidity, wind speed, air pressure, and incoming and outgoing radiation fluxes (Table 1). Surface height was measured using ultrasonic depth gauges (UDGs) next to the corresponding AWS. The UDGs were installed between 0.5 and 2 m over the glacier surface on metallic frames. The frames consisted of 3–4 m horizontal aluminum pipes supported by two vertical tubes drilled into the ice surface. Precipitation was not measured, but solid precipitation was estimated using variations of surface height and albedo. Meteorological stations at lower valleys and albedo records suggest that most precipitation events during the study period were occasional and of little magnitude. Air temperature and relative humidity sensors were artificially aspirated, except for that on Guanaco Glacier. However, as strong winds have been reported at this site [*MacDonell et al.*, 2013], we did not correct these measurements. As the instruments were placed on sites with local slopes below 5°, we did not perform any correction for tilt

**Table 2.** Initial Conditions and Validation Metrics of the EB Model Calculated From the Observed and Simulated Surface Temperature[a]

| Glacier and Season | Initial Snow Depth (m) | Initial Average Snow Density (kg m$^{-3}$) | Surface Temperature Validation | | |
|---|---|---|---|---|---|
| | | | *NS* | *RMSE* (°C) | *MBD* (°C) |
| JN3127 2008–2009 | 0.0 | | | | |
| JN3305 2008–2009 | 0.7 | 481 | | | |
| SF3466 2013–2014 | 2.0* | 520* | 0.68 | 1.09 | −0.51 |
| SF3466 2014–2015 | 1.7* | 520* | 0.65 | 1.20 | −0.44 |
| BE4134 2013–2014 | 2.0 | 520 | 0.87 | 1.30 | 0.05 |
| BE4134 2014–2015 | 1.7 | 520* | 0.90 | 1.21 | 0.05 |
| YE4428 2013–2014 | 2.0* | 520* | 0.90 | 1.29 | 0.05 |
| YE4428 2014–2015 | 1.7* | 520* | 0.88 | 1.79 | 0.67 |
| TA4775 2013–2014 | 1.1 | 450 | 0.96 | 0.87 | −0.34 |
| GU5324 2008–2011 | 0.0 | | 0.92 | 1.78 | 0.72 |

[a]Grey and blank areas are added to distinguish between glaciers. The values of snow density and initial snow depth marked with * were inferred from BE4134 (the snow density measured on 2013–14 was also used in 2014–15).

to the incoming shortwave radiation record. Air pressure was measured at all sites except on Guanaco and Juncal Norte Glacier. On Guanaco Glacier, we used air pressure from a nearby station [*MacDonell et al*., 2013] and on Juncal Norte Glacier it was estimated as a function of elevation. This was also the case for the AWS on Tapado Glacier, where air pressure measurements had significant errors. AWSs and UDGs were inspected every 4–8 weeks.

At the time of the AWSs installation, snow pits were dug on Juncal Norte, Bello, and Tapado glaciers. The snow density values measured on Bello Glacier were used on Yeso and San Francisco glaciers, and no snow was present on Guanaco Glacier at the start of the study period (Table 2). Ablation stakes were installed on Juncal Norte, Bello, and Tapado glaciers and readings were performed during the visits to the AWSs. Penitentes developed at the AWSs sites of Tapado and Yeso glaciers. In order to obtain an average surface lowering of the penitentes surface at Tapado Glacier, we measured the distance from a horizontal aluminum pipe (similar to that of the UDG) to the surface every 20 cm. The average surface lowering was calculated as the average of measurements along the horizontal pipe. The pipes were reinstalled and measurements of surface lowering were performed when the AWS was visited. *Nicholson et al*. [2016] have recently showed that, although this type of manual point measurements cannot capture complex morphological changes of penitentes, they produce similar estimates of mean surface lowering compared to more complex methods of surface mapping.

## 3. Methods

### 3.1. Energy Balance (EB) Model

We use the AWS data to force a multilayer EB model that includes physically based equations of the main processes affecting the glacier surface. The energy balance equation for the top or surface layer ($i=1$) is:

$$\int_0^{z_1} \rho c_s \frac{\partial T_{i=1}}{\partial t} dz = \xi S_{net} + L_{net} + Q_H + Q_L + Q_{C(i=1)} + Q_{M(i=1)} + Q_{R(i=1)} \quad (1)$$

where $i$ is the layer number, $\rho$ is the snow or ice density (kg m$^{-3}$), $c_s$ is the heat capacity (J kg$^{-1}$ K$^{-1}$), $T_{i=1}$ is the snow or ice temperature of the top layer (K), $z$ is the vertical axis (positive downward), $S_{net}$ is the net shortwave radiation, $\xi$ is the fraction of $S_{net}$ absorbed in the surface layer, $L_{net}$ is the net longwave radiation, $Q_H$ is the turbulent sensible heat flux, and $Q_L$ is the turbulent latent heat flux. $Q_{C(i=1)}$, $Q_{M(i=1)}$, and $Q_{R(i=1)}$ are the conductive heat flux, the latent heat from melt, and the latent heat from refreezing in the top layer, respectively. The energy balance for a subsurface layer $i$ is:

$$\int_{z_{i-1}}^{z_i} \rho c_s \frac{\partial T_i}{\partial t} dz = S_{net}(1-\xi)\left(e^{-\beta(z_{i-1}-z_1)} - e^{-\beta(z_i-z_1)}\right) + Q_{C(i)} + Q_{M(i)} + Q_{R(i)} \quad (2)$$

where $\beta$ is a decay coefficient for the shortwave radiation within the snow or ice (m$^{-1}$). In equation (2), the first term on the right side represents the absorption in layer $i$ of $S_{net}$ that penetrates the snow/ice below the top layer ($S_{net}(1-\xi)$) [*Bintanja and van den Broeke*, 1995]. The remaining terms are analogous to those in equation (1). $\xi$ corresponds to 1 for new snow, 0.9 for snow, and 0.8 for ice and $\beta$ is 17.1 m$^{-1}$ for all type

of snow and 2.5 $m^{-1}$ for ice [*Mölg et al.*, 2012]. Albedo is not parameterized and its values are directly derived from measurements of incoming and reflected shortwave radiation. Conductive heat fluxes are calculated as:

$$Q_C = K\frac{\partial T}{\partial z} \tag{3}$$

where $K$ is thermal conductivity, which is calculated as a function of density in the case of snow and assumed as 2.07 $Wm^{-1}K^{-1}$ in the case of ice [*Sturm et al.*, 1997; *Pellicciotti et al.*, 2009]. If the temperature of a layer reaches 0°C in equations (1) and (2), the latent heat from melt is calculated as the residual of the energy balance equation. Total melt ($M$) in the vertical profile is calculated as:

$$M = \frac{\sum_i Q_{Mi}}{\lambda_f \rho_w} \tag{4}$$

where $Q_{Mi}$ is the energy available for melt at layer $i$ (W $m^{-2}$), $\lambda_f$ is the latent heat of fusion ($3.34 \cdot 10^5$ J $kg^{-1}$), and $\rho_w$ is the density of water.

We include a module for the storage and refreezing of liquid water within the snowpack, where the gravitational movement of liquid water occurs when a snow layer reaches its maximum storage capacity, which is a function of snow density [*Anderson*, 1976; *Essery et al.*, 2013]. Excess meltwater is converted to runoff when all layers in the snowpack are saturated. Refreezing of meltwater occurs at snow layers when the layer temperature drops below 0°C and the liquid content is more than zero. The measured snow densities are used as initial conditions and we increase the density of each snow layer by adding the corresponding refrozen water mass. A value of 60 kg $m^{-3}$ is used for the density of new snow [*MacDonell et al.*, 2013]. We consider the surface as new snow when the measured albedo is higher than 0.8.

The EB model calculates surface temperature ($T_1$) as a result of equation (1) and outgoing longwave radiation using the Stefan-Boltzmann equation:

$$L_{out} = \epsilon \sigma T_1^4 \tag{5}$$

where $L_{out}$ is outgoing longwave radiation (W $m^{-2}$), $\epsilon$ is surface emissivity (taken equal to 1), and $\sigma$ is the Stefan-Boltzmann constant ($Wm^{-2}K^{-4}$). As $\epsilon$ is assumed equal to 1, $L_{out}$ entirely corresponds to emitted radiation by the surface. As incoming longwave radiation was not measured at Juncal Norte Glacier, we calculate it following the parameterization of *Prata* [1996], which depends on air temperature, precipitable water, and air pressure. This method has been suggested as appropriate for dry climates [*Niemelä et al.*, 2001] and has been used at this site previously [*Pellicciotti et al.*, 2008].

Turbulent heat fluxes are calculated using a first-order closure of the turbulence, a stability correction based on the similarity theory of *Monin and Obukhov* [1954] and the parameterization of aerodynamic surface roughness length for temperature and humidity proposed by *Andreas* [1987]. Despite the fact that several of its assumptions are not valid over glacier slopes, it has been shown that a bulk-formulation of the Monin-Obukhov stability correction provides reasonable results on glacier surfaces where a stable stratification forms [*Denby and Greuell*, 2000] and it has been widely used in glaciological research [e.g., *Brock et al.*, 2006; *Winkler et al.*, 2009]. The turbulent heat fluxes are calculated as:

$$Q_H = \rho_{air} \cdot c_p \cdot k^2 \cdot WS \cdot \frac{T_a - T_1}{\left(\ln\left(\frac{z_{ins}-d_0}{z_0}\right) - \Psi_m\right) \cdot \left(\ln\left(\frac{z_{ins}-d_0}{z_t}\right) - \Psi_t\right)} \tag{6}$$

$$Q_L = \rho_{air} \cdot \lambda_v \cdot k^2 \cdot WS \cdot \frac{q_a - q_1}{\left(\ln\left(\frac{z_{ins}-d_0}{z_0}\right) - \Psi_m\right) \cdot \left(\ln\left(\frac{z_{ins}-d_0}{z_q}\right) - \Psi_q\right)} \tag{7}$$

where $\rho_{air}$ is air density (1.26 kg $m^{-3}$), $c_p$ is the specific heat of air (J $kg^{-1}$ $K^{-1}$), $k$ is the Von Karman constant (0.4), $WS$ is wind speed (m $s^{-1}$), $\lambda_v$ is the latent heat of vaporization/sublimation (J $kg^{-1}$), $q_a$ and $q_1$ are the specific humidity of air and glacier surface, $z_{ins}$ is the instrumental height (m), $d_0$ is the displacement length (m), $z_0$, $z_t$, and $z_q$ are the surface roughness length for momentum, temperature and humidity (m), and $\Psi_m$, $\Psi_t$, and $\Psi_q$ are the vertically integrated stability correction functions. The complete formulation of the turbulent fluxes equations used in this study can be found in *Carenzo* [2012] and *Dadic et al.* [2012]. We use a

$z_0$ value of 0.1, 1, and 2 mm for new snow, snow, and ice, respectively [*Pellicciotti et al*., 2005]. Negative values of $Q_L$ are converted to surface sublimation if $T_1 < 0°C$ or to evaporation if $T_1 = 0°C$. In the same way, positive values of $Q_L$ are converted to deposition or condensation [*Hock and Holmgren*, 2005]. The displacement length is calculated as linear function of $z_0$ [*Brutsaert*, 1982; *Corripio*, 2003; *Dadic et al*., 2012]. Penitentes are not modeled explicitly, but we use a $z_0$ value of 0.2 m to include their effect on the turbulent fluxes at Tapado and Yeso glaciers. This value of $z_0$ was estimated by *Corripio and Purves* [2005] for fully developed penitentes in the semiarid Andes of Central Chile and is in the range of computations performed by *Nicholson et al*. [2016] for the same site at Tapado Glacier (0.10–0.50 m).

Blowing snow sublimation is calculated from the saltation and suspension layers using a 1-D adaptation of the equations of the SnowTran-3-D model [*Liston and Sturm*, 1998], which uses several of the equations proposed by *Pomeroy et al*. [1993]. While the wind speed threshold for snow transport is defined as a function of air temperature in the case of dry snow [*Li and Pomeroy*, 1997], we neglect the snow transport from a snow surface that has been exposed to air temperatures higher than 0°C (wet snow). As we only perform a point-scale simulation, the lateral advection of snow in the saltation and suspension layers is neglected in the equations. We do not have direct observations of the occurrence of blowing snow episodes to validate this model component, but we decided to include this module, the equations of which have been tested in different climatic settings [e.g., *Liston and Sturm*, 1998; *Strasser et al*., 2008; *Gascoin et al*., 2013], to provide an estimation of the amounts of blowing sublimation during the ablation season on these glaciers. We keep these calculations as a reference value and we do not include the calculated values of blowing snow sublimation in the simulated surface ablation.

The EB model is run with an hourly time step at every site except at Tapado and San Francisco glaciers, where available measurements at 10 min intervals are used. A subtime step of one minute is used at every site to avoid numerical instabilities in the calculation of heat conduction and latent heat fluxes within the snow and ice. The Crank-Nicolson method is used to numerically solve the heat conduction. We discretize the first 10 cm of the initial snow height in 2.5 cm layers, the remaining snow depth in 25 cm layers, and the ice column in 3 m layers. If at the starting time of the simulations there is no accumulated snow, we discretize the first 10 cm of ice in layers of 2.5 cm, the next meter in layers of 25 cm and the remaining ice column in layers of 3 m. When the simulated cumulative ablation (accumulation) amounts to more than 2.5 cm, the top layer is removed (added) and the snow and ice profiles are updated accordingly. We keep the initial number of layers constant through the simulation period and we used a boundary condition for temperature at a depth of 15 m at each study site. This temperature was measured at Guanaco Glacier (–6.5°C) [*MacDonell et al*., 2013] and it is estimated as −5°C for the rest of the study sites. EB model outputs are validated using ablation stakes, the continuous UDG surface height records, and $L_{out}$ measurements, from which we estimate surface temperature using a surface emissivity of 1. The initial snow height and density used at each site are provided in Table 2.

As some of the EB model parameters are not measured in the field, or are not measured at every site and season (the case of snow density), we perform an uncertainty and sensitivity analysis to: (i) quantify the uncertainty in ablation rates given a range of possible values of the EB model parameters, and (ii) identify the parameters to which ablation rates are most correlated. For this, we select five EB model parameters: $z_0$, $\rho_s$, $\epsilon$, $\xi$, and $\beta$. A detailed description of the methodology and results of this analysis is provided in the supporting information, and just the main results are summarized in the following sections.

### 3.2. Enhanced Temperature Index (ETI) Model

The ETI model can be understood as a simplified energy balance model where the energy available for melt is calculated as a function of the shortwave radiation balance and air temperature [*Pellicciotti et al*., 2005]. The model has been previously applied in diverse mountain environments, including the semiarid Andes [*Pellicciotti et al*., 2008; *Ragettli et al*., 2016], the Alps [*Finger et al*., 2011; *Gabbi et al*., 2014], and Himalaya [*Ragettli et al*., 2013, 2015]. While the shortwave radiation balance is treated explicitly as an individual term, the longwave radiation balance, turbulent fluxes, and internal heat fluxes are aggregated into a term linearly related to air temperature:

$$M=\begin{cases} SRF \cdot S_{in} \cdot (1-\alpha)+TF \cdot T_a & T_a > T_T \\ 0 & T_a \leq T_T \end{cases} \quad (8)$$

where $M$ is melt (mm $h^{-1}$), $SRF$ is a shortwave radiation factor (mm $h^{-1}$ $W^{-1}$ $m^2$), $S_{in}$ is incoming shortwave radiation (W $m^2$), $\alpha$ is the surface albedo, $TF$ is a temperature factor (mm $h^{-1}°C^{-1}$), $T_a$ is air temperature (°C), and $T_T$ is the temperature threshold for melt onset (°C). In time steps when $T_T$ is below 0°C and air temperature is between $T_T$ and 0°C, we set the contribution of melt from the temperature term to zero. In this way, the ETI model is able to simulate melt during periods with air temperatures below 0°C and strong $S_{in}$, which is a meteorological condition typical of high-elevation sites in the semiarid Andes.

We calibrate the ETI parameters against hourly melt rates simulated by the EB model for the entire period (seasonally calibrated ETI) and separately for each month with more than 15 days of data available (monthly calibrated ETI). The optimal parameter set is selected as the one that provides the maximum Nash-Sutcliffe value.

In order to evaluate the transferability in space and time of the ETI parameters, we define a cross-validation procedure in which we force the ETI model with input variables from one site and season and seasonally calibrated parameters from the remaining sites. Subsequently, we further evaluate the performance of the ETI model in two ways. First, we study the ability of the air temperature threshold approach to identify the onset of melt. In this analysis, we calculate the portion of melt simulated by the ETI model on time steps when the EB model does not simulate melt and vice versa. In this way, we define an error type 1 (T1), or false positive, as the situation when there is no energy available for melt, i.e., the EB model does not simulate melt, but the air temperature is above $T_T$, i.e., the ETI model prescribes melt. Analogously, we define an error type 2 (T2), or false negative, as the absence of melt in the ETI model in time steps when there is energy available for melt. Second, we study the relation between melt, energy inputs to the glacier surface and meteorological variables using the Pearson correlation coefficient. For this, we define the temperature-dependent fraction of the energy inputs ($\Phi$), similar to the approach of *Pellicciotti et al.* [2008] and *Giesen and Oerlemans* [2012], as:

$$\Phi=L_{in}+Q_H+Q_L \quad (9)$$

where $L_{in}$ is incoming longwave radiation.

### 3.3. Metrics of Model Evaluation

We use as metrics to compare reference and simulated values the Nash-Sutcliffe (*NS*) coefficient, the Root Mean Square Error (*RMSE*), and the Mean Bias Difference (*MBD*). As the *RMSE* is a well-known metric, we provide here only the equations of *NS* and *MBD*:

$$NS=1-\frac{\sum_{i=1}^{n}(y_{SIM\ i}-y_{OBS\ i})^2}{\sum_{i=1}^{n}(y_{OBS\ i}-\overline{y_{OBS}})^2} \quad (10)$$

$$MBD=\frac{1}{n}\sum_{i=1}^{n}(y_{SIM\ i}-y_{OBS\ i}) \quad (11)$$

where $y_{SIM}$ and $y_{OBS}$ are the simulated and observed values and $n$ is the length of the sample.

## 4. Results

### 4.1. Meteorological Measurements

Figure 2 shows comparison of meteorological input variables at each glacier, during the main part of the ablation season (November–February). Although Figure 2 compares monthly averages calculated over different seasons in the period 2008–2015 (see Table 1 for the period of record of each AWS), it provides an overview of the dominant meteorological conditions at each site. Hereafter study sites are arranged by their elevation. Air temperature exhibits a clear relation with elevation in each month, with exceptions in January for Bello, Tapado, and Yeso glaciers (Figure 2a). Relative humidity varies between 30 and 60% across the study region, but there is no clear relation to elevation or latitude (Figure 2b). Whereas monthly averaged

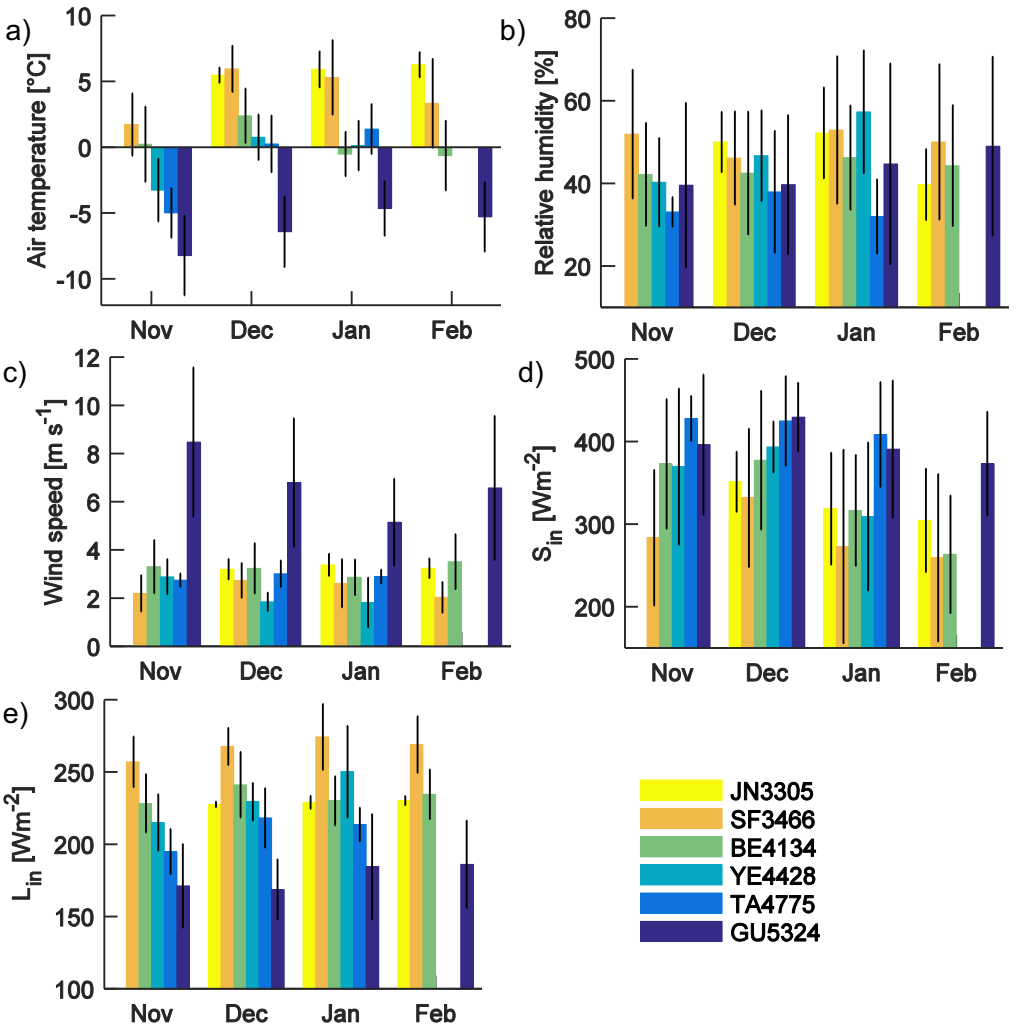


**Figure 2.** Monthly mean (color bars) and standard deviation derived from daily mean values (black vertical lines) of (a) air temperature, (b) relative humidity, (c) wind speed, (d) incoming shortwave radiation ($S_{in}$), and (e) incoming longwave radiation ($L_{in}$) at each glacier for the period November–February. Monthly mean values were calculated as the average over different years depending on data availability (see Table 1). Wind speed data from Guanaco Glacier were transferred to a 2 m height using the logarithmic profile used in the EB model. See site codes in Figure 1.

values are relatively stable at each site during summer, daily values of relative humidity have a large variability within each month (Figure 2b). Wind data do not show large differences from site to site (Figure 2c), with the exception of GU5324 where wind speed is significantly higher than at the rest of the study sites. $S_{in}$ increases with increasing elevation, but this can also be explained by differences in cloudiness and potential $S_{in}$ between the North and Central Chile clusters (Figure 2d). $L_{in}$ has a decreasing trend with elevation (Figure 2e), which is a consequence of the lower air temperature and the larger atmospheric transparency due to the lower water vapor content at higher elevations [*Marty et al.*, 2002]. $L_{in}$ estimated for Juncal Norte Glacier is lower than what can be expected from the observed regional trend, suggesting that either the tongue of Juncal Norte Glacier has a more cloud-free condition than the other sites (Figure 2d) or the selected parameterization [*Prata*, 1996] underestimates $L_{in}$ and a parameter recalibration might be necessary.

### 4.2. Energy Balance Model

#### 4.2.1. Validation

Variations in surface height are well reproduced by the EB model (Figure 3), with the exception of some errors at sites above 4000 m a.s.l. (Figures 3e–3i) and toward the end of the observation periods at BE4134 and YE4428 in 2013–2014 (Figures 3d–3f). Unfortunately, UDGs did not work during the entire ablation season at several sites (Figures 3c, 3d, 3e, and 3g). Some of the errors are likely caused by a wrong

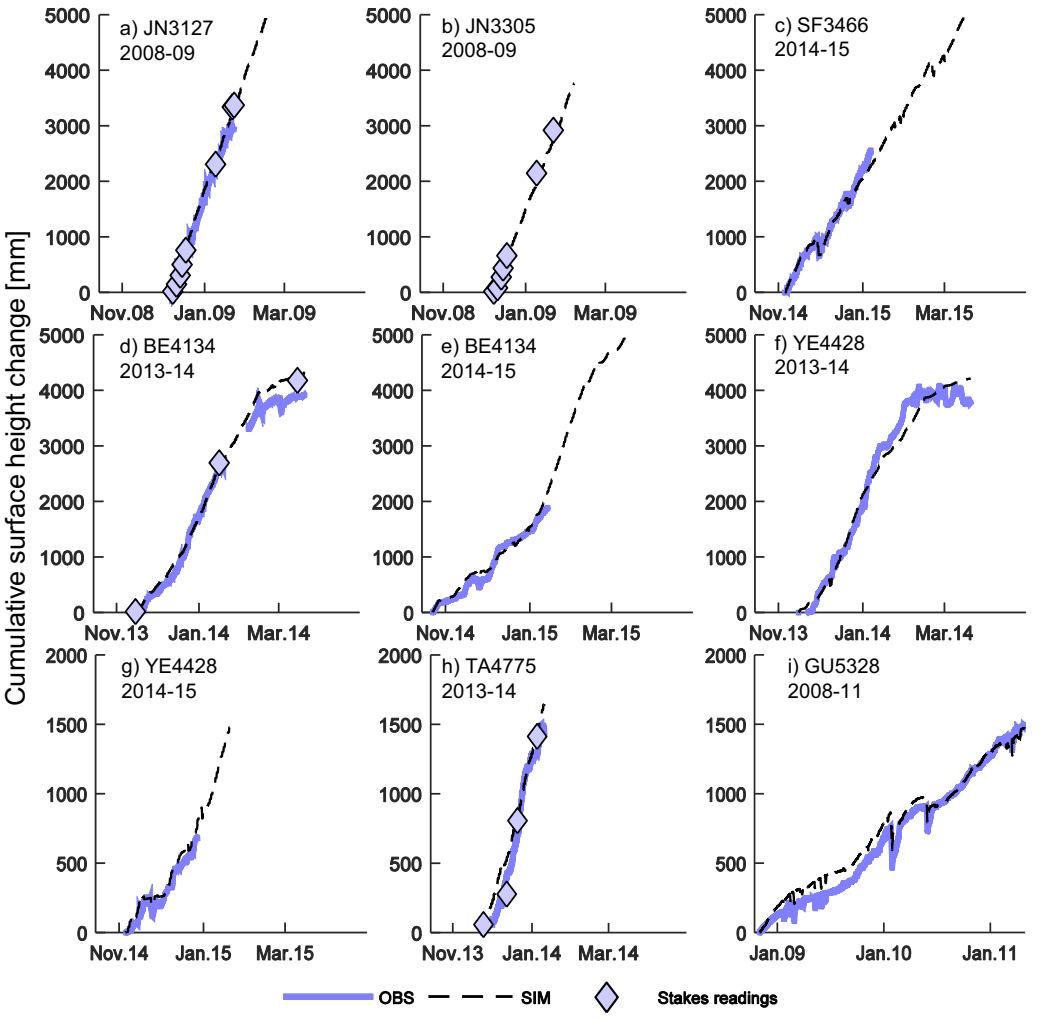


**Figure 3.** Comparison of observed (OBS) and EB simulated (SIM) cumulative values of hourly surface height change at sites with surface height sensors and/or ablation stake readings. (a)–(h) The same time period in the *x* axis is used (15 October to 30 April of corresponding years) and the ticks show the first day of each month. (i) The entire time extent of data collected at GU5324 is shown in the *x* acis (November 2008 to April 2011) and the ticks show the first day of each year. Note that, to facilitate the comparison between observed and simulated values, the *y* axis of the Figures 3g, 3h, and 3i have a different upper limit than at the rest of the plots.

representation of occasional snowfalls (Figures 3e, 3f, 3g, and 3i) or periods when the glacier surface increases its roughness (Figures 3d, 3g, and 3h). At GU5328, ablation was overestimated during a short period at the beginning of the simulation period and this error is carried for that entire year, though simulated and observed curves are parallel most of the time.

Table 2 shows that simulated and observed surface temperature values are also in good agreement (Table 2). *RMSE* ranges between 0.87 and 1.79°C while *NS* ranges between 0.65 and 0.96. *MBD* values are below 0.72°C in absolute terms and are both positive and negative, which suggests that the model does not systematically over or underestimate surface temperature. During the season 2014–2015, the EB model correctly reproduces surface elevation changes at SF3466 (Figure 3c), but simulated and observed values of surface temperature show one of the lowest agreements of all sites and seasons (Table 2). This might be caused by a number of reasons, including sensor biases and surface conditions that are not well represented by the values of the model parameters, particularly surface emissivity, heat capacity, thermal conductivity, and snow density.

#### 4.2.2. Energy and Summer Mass Balance

Figure 4 shows monthly average surface energy fluxes and albedo at different times of the ablation season at each study site. The aim of this figure is to show how the altitudinal patterns of surface energy fluxes and

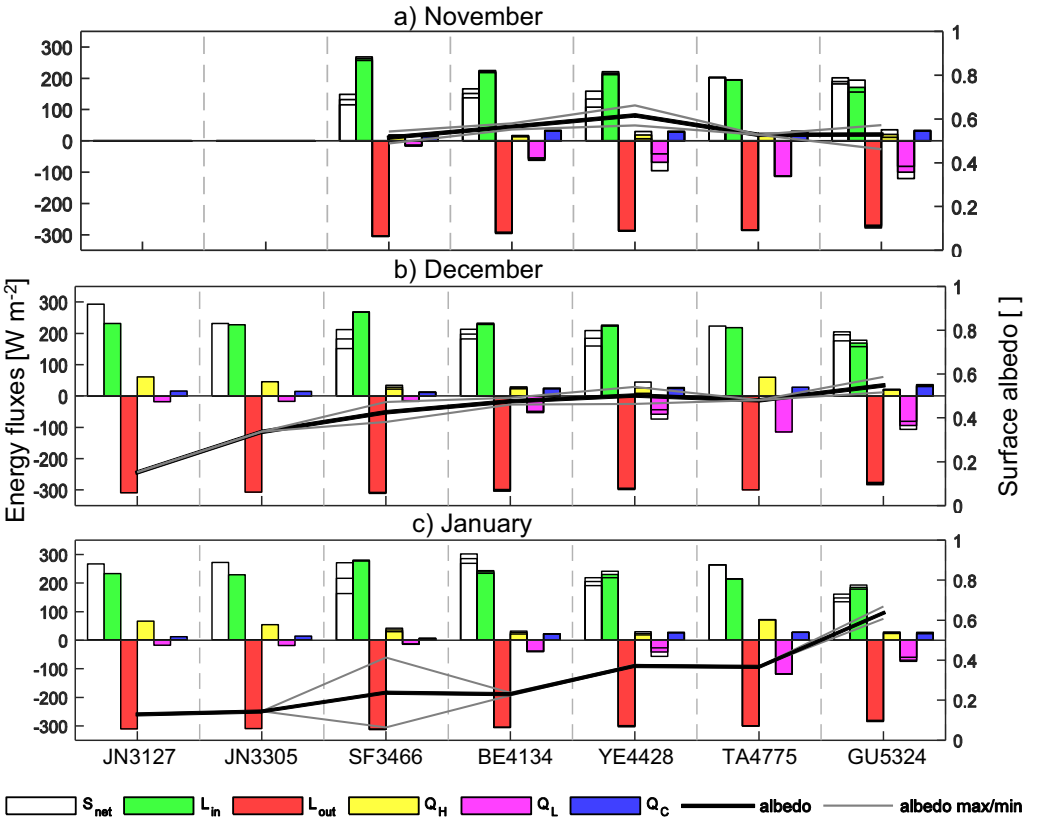


**Figure 4.** Average surface energy fluxes (left axis) and surface albedo (right axis) in (a) November, (b) December, and (c) January at each study site and season. Energy fluxes are net shortwave radiation ($S_{net}$), incoming longwave radiation ($L_{in}$), outgoing longwave radiation ($L_{out}$), turbulent sensible heat flux ($Q_H$), turbulent latent heat flux ($Q_L$), and conductive heat fluxes to the surface layer ($Q_C$). At sites with data available for more than one season, we show the maximum and minimum monthly mean value as upper and lower lines above and below the average value.

albedo evolve over the ablation season. As an indication of the interannual variability, the maximum and minimum monthly mean values calculated for sites with data available for more than one season are also shown. In November (Figure 4a), albedo is relatively uniform across the available sites and varies between 0.5 and 0.65. $L_{in}$ and $S_{net}$ are the largest energy inputs to the glacier and have a decreasing and increasing trend with elevation, respectively. The trend of $L_{in}$ can be explained by a colder air temperature and a lower humidity at higher elevations and the trend in $S_{net}$ can be explained by a decrease in cloudiness and an increase in potential $S_{in}$ at lower latitudes (see Figures 2a, 2b, and 2d). $Q_H$ is positive and $Q_L$ is negative at all study sites. Their magnitudes are similar at SF3466, but while $Q_H$ remains relatively uniform, $Q_L$ strongly decreases with elevation from $-15$ to $< -100$ W m$^{-2}$. As the ablation season advances (Figures 4b and 4c), albedo decreases at all sites except at GU5324, where it slightly increases in January due to occasional snowfalls. At each site, the decrease in albedo produces an increase of $S_{net}$. $Q_H$ is largest at the sites on the tongue of Juncal Norte Glacier, due to the afternoon advection of warm air from the proglacial valley [*Petersen and Pellicciotti*, 2011; *Ayala et al*., 2015], and at TA4775, due to the large surface roughness associated with penitentes (Figure 2b). $Q_C$ is positive and relatively small at the average monthly scale, though its diurnal variation might show large positive and negative values. $L_{out}$ tends to decrease with elevation due to colder surface temperatures, but its variations are smaller than those of the rest of the energy fluxes. The interannual differences in energy fluxes and albedo are small and do not modify the described altitudinal patterns, with the exception of SF3466, where the seasonal snow cover disappeared earlier in summer 2014–2015 than in the previous year, exposing the ice and producing a low albedo in January.

Using the same structure as Figure 4, Figure 5 presents the most relevant mass balance components as a percentage of total ablation. Hereafter, we refer to total ablation as the sum of melt, evaporation, and surface sublimation. In November (Figure 5a), total ablation has a dominant decreasing trend with elevation

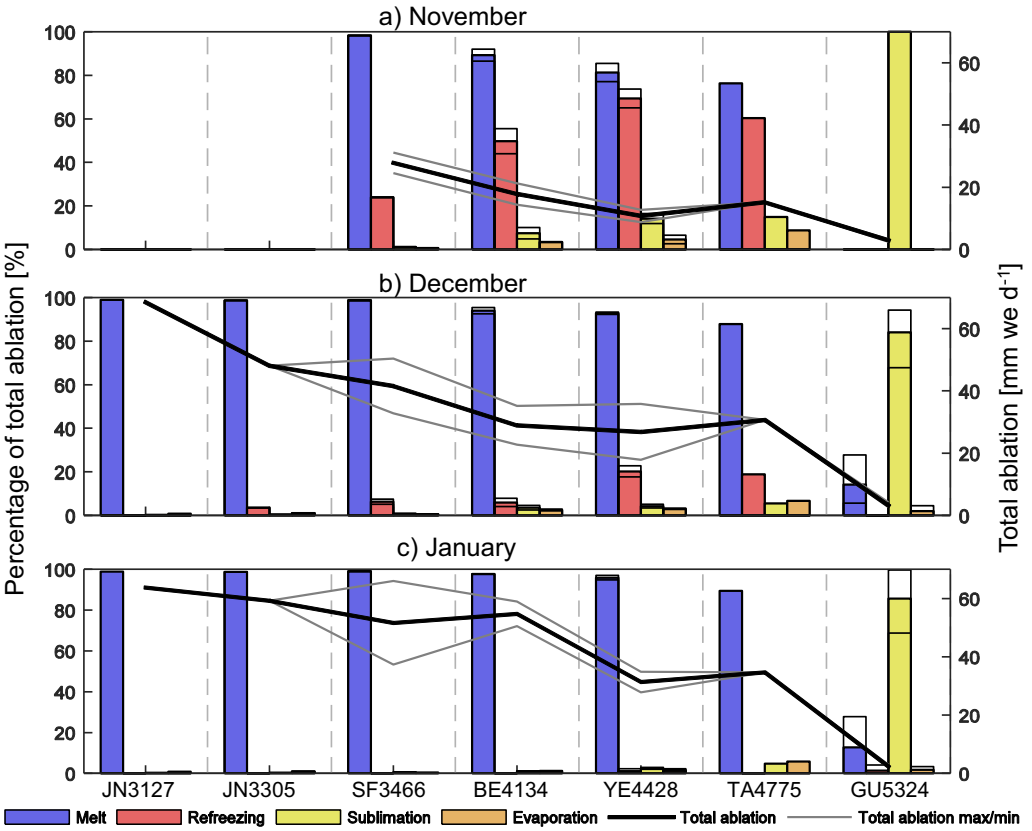


**Figure 5.** Most relevant mass balance components during (a) November, (b) December, and (c) January. Left axis shows the percentage that each component represents of total ablation (considered as the sum of melt, surface sublimation and evaporation). Right axis shows the daily average of total ablation. Precipitation, condensation, deposition, and blowing snow sublimation are not shown due to their low values. At sites with data available for more than one season, we show the maximum and minimum monthly mean value as upper and lower lines above and below the average value.

from 28 mm water equivalent (w.e.) $d^{-1}$ at SF3466 to 3 mm w.e. $d^{-1}$ at GU5324. Melt almost completely dominates ablation at SF3466, but consistently decreases from nearly 100 to 0% of total ablation at higher elevations. Surface sublimation has an increasing role with elevation and completely dominates ablation at GU5324, due to its cold temperature, low air pressure, and strong winds (Figures 2a–2c). Refreezing values are equivalent to 23% of total ablation at SF3466 and increase with elevation up to 73% at YE4428. At GU5324 refreezing is close to zero because there is no meltwater available. As the ablation season advances (Figures 5b and 5c), total ablation tends to increase, melt almost completely dominates ablation, the relative importance of refreezing decreases, and surface sublimation is only relevant at the highest sites. Evaporation occurs at sites with available meltwater and large negative $Q_L$. The decrease of refreezing along the season is associated with the disappearance of the snowpack or a reduction of its cold content, which results in an increase of the effective meltwater runoff. The interannual differences are largest at SF3466, where the low-albedo ice was exposed at different times of the summer season during the analyzed years (see Figure 4c).

In Table 3, we further analyze the variation of midsummer ablation rates by comparing daily average rates of melt, surface sublimation, and evaporation. Melt decreases with elevation from 67.2 mm w.e. $d^{-1}$ at JN3127 to values between 25 and 35 mm w.e. $d^{-1}$ at YE4428 and TA4775. At GU5324, melt sharply decreases to values below 1 mm w.e. $d^{-1}$. Surface sublimation has a general increasing trend with elevation from values smaller than 0.5 mm w.e. $d^{-1}$ at JN3127 and SF3466 to values larger than 1.5 mm w.e. $d^{-1}$ at TA4775 and GU5324. Evaporation rates are generally below 1 mm w.e. $d^{-1}$, with the exception of TA4775, where a combination of available meltwater and large negative latent fluxes associated with the rough surface produces rates of 2 mm w.e. $d^{-1}$. As the other mass balance components, such as precipitation, deposition, and blowing snow sublimation, are considerably smaller than melt, surface sublimation, and

**Table 3.** Average Rates of Melt, Surface Sublimation, and Evaporation at Each Site During the Period December–January of Each Ablation Season[a]

| Glacier Season | Melt (mm w.e. $d^{-1}$) | Surface Sublimation (mm w.e. $d^{-1}$) | Evaporation (mm w.e. $d^{-1}$) |
|---|---|---|---|
| JN3127 2008–2009 | 67.2 | 0.2 | 0.5 |
| JN3305 2008–2009 | 58.5 | 0.2 | 0.6 |
| SF3466 2013–2014 | 65.5 | 0.3 | 0.2 |
| SF3466 2014–2015 | 36.9 | 0.3 | 0.1 |
| BE4134 2013–2014 | 49.3 | 0.6 | 0.6 |
| BE4134 2014–2015 | 57.6 | 0.6 | 0.7 |
| YE4428 2013–2014 | 33.1 | 1.0 | 0.8 |
| YE4428 2014–2015 | 26.9 | 0.5 | 0.3 |
| TA4775 2014–2015 | 31.1 | 1.6 | 2.0 |
| GU5324 2008–2009 | 0.2 | 1.7 | 0.0 |
| GU5324 2009–2010 | 0.8 | 2.0 | 0.1 |
| GU5324 2010–2011 | 0.0 | 2.2 | 0.0 |

[a]Grey and blank areas are added to distinguish between glaciers.

evaporation, we do not present them here. For a full comparison of energy fluxes and ablation rates, see supporting information Table S1.

Results of the uncertainty and sensitivity analysis (see supporting information for details) show that parameter uncertainty in the EB model produces small variations in surface sublimation (<1 mm w.e. $d^{-1}$) and melt rates (<12 mm w.e. $d^{-1}$). In relative terms, these variations are generally small (<4% in melt and <8% in surface sublimation), but they can be large at sites with small ablation rates (65% in melt and 28% in surface sublimation). From the five selected parameters ($z_0$, $\rho_s$, $\epsilon$, $\xi$, and $\beta$), we only find significant correlations (>0.93) between $z_0$ and the ablation rates.

### 4.3. ETI Model

#### 4.3.1. Model Parameters and Transferability

The optimal values of the ETI parameters are shown in Table 4 and analyzed in Figure 6. In Figure 6, we plot their distribution and main properties, except for GU5324, for which the low performance of the model does not grant drawing meaningful conclusions. We find a clear relation between $T_T$ and average air temperature for seasonally (Figure 6a) and monthly (Figure 6b) calibrated parameters. In general, warm temperatures are associated with large values of $T_T$. In Figures 6c and 6d, we show the distribution across sites of seasonally and monthly calibrated parameters with error bars

**Table 4.** Parameters and Validation Metrics of the ETI Model[a]

| | | | Seasonally Calibrated ETI Parameters (Ranges for the Optimal Values are Shown in Parenthesis) | | | Validation Metrics Seasonally Calibrated ETI (Entire Season) | | | Validation Metrics Monthly Calibrated ETI (Entire Season) | | |
|---|---|---|---|---|---|---|---|---|---|---|---|
| Glacier | AWS | Season | *SRF* (mm $h^{-1}$ $W^{-1}$ $m^2$) *$10^{-4}$ | *TF* (mm $h^{-1}$ °C) *$10^{-4}$ | $T_T$ (°C) | *NS* | *RMSE* (mm $h^{-1}$) | *MBD* (mm $h^{-1}$) | *NS* | *RMSE* (mm $h^{-1}$) | *MBD* (mm $h^{-1}$) |
| Juncal Norte | JN3127 | 2008–2009 | 99 (85–108) | 100 (0–750) | 5.5 | 0.98 | 0.57 | 0.06 | 0.98 | 0.56 | 0.03 |
| | JN3305 | 2008–2009 | 99 (83–101) | 0 (0–400) | 4.0 | 0.97 | 0.62 | 0.10 | 0.97 | 0.60 | 0.09 |
| San Francisco | SF3466 | 2013–2014 | 100 (87–108) | 50 (50–550) | 2.0 | 0.97 | 0.50 | 0.02 | 0.98 | 0.48 | 0.01 |
| | | 2014–2015 | 94 (83–101) | 0 (50–250) | 1.5 | 0.97 | 0.44 | 0.03 | 0.97 | 0.42 | 0.04 |
| Bello | BE4134 | 2013–2014 | 67 (57–76) | 950 (300–1800) | −1.5 | 0.87 | 0.84 | 0.16 | 0.90 | 0.72 | 0.11 |
| | | 2014–2015 | 74 (64–82) | 400 (150–950) | −1.5 | 0.89 | 0.83 | 0.15 | 0.92 | 0.72 | 0.10 |
| Yeso | YE4428 | 2013–2014 | 50 (42–57) | 2400 (2050–2950) | −1.5 | 0.83 | 0.81 | 0.11 | 0.87 | 0.72 | 0.07 |
| | | 2014–2015 | 54 (46–62) | 1400 (850–2000) | −2.5 | 0.78 | 0.72 | 0.09 | 0.80 | 0.68 | 0.05 |
| Tapado | TA4775 | 2013–2014 | 41 (34–47) | 2450 (2050–3100) | −3.5 | 0.82 | 0.73 | 0.15 | 0.83 | 0.70 | 0.11 |
| Guanaco | GU5324 | 2008–2011 | 6 (5–7) | 200 (100–300) | 1.0 | 0.16 | 0.10 | 0.00 | 0.41 | 0.13 | 0.00 |

[a]Values of the validation metrics are calculated by comparing hourly melt rates from the ETI model with those of the EB model. Optimal values of the seasonally calibrated *SRF* and *TF* are provided with the ranges that produce variations of 1% in the optimal NS value. Grey and blank areas are added to distinguish between glaciers.

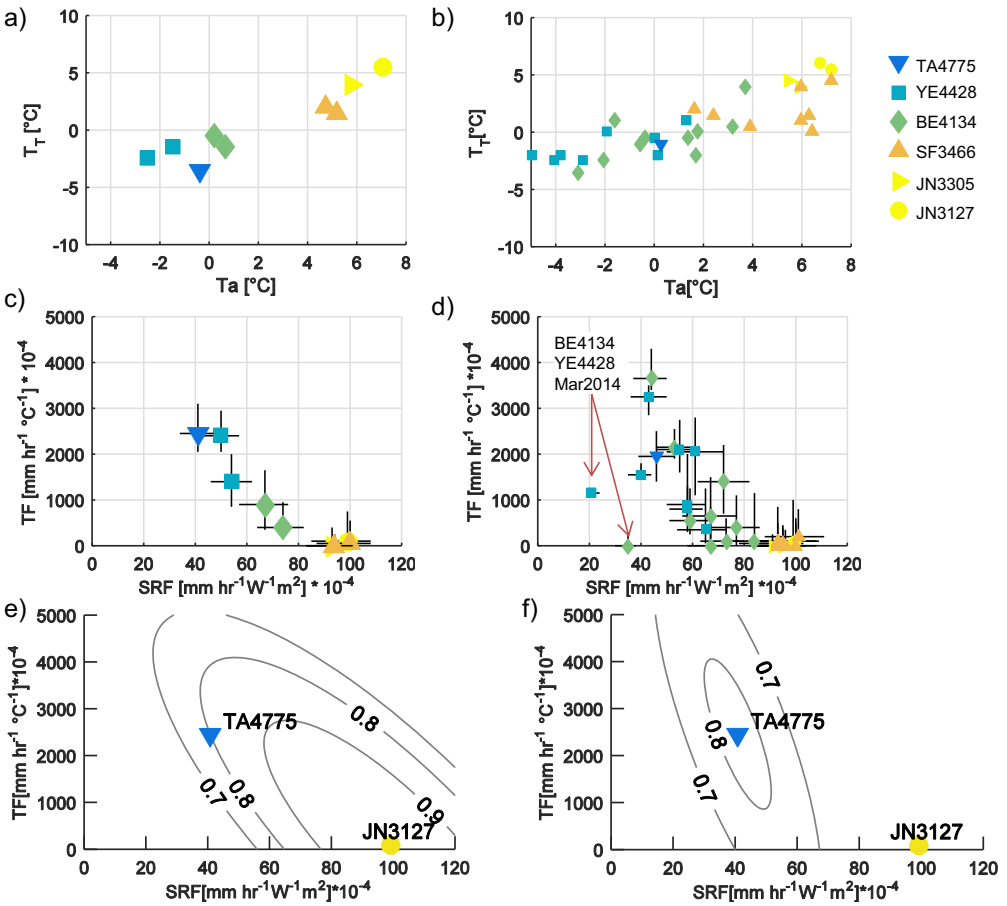


**Figure 6.** (a and b) Optimal values of $T_T$ as a function of average air temperature for (a) seasonally calibrated and (b) monthly calibrated parameters. (c and d) Optimal values of *TF* and *SRF* for (c) seasonally calibrated and (d) monthly calibrated parameters. Markers show the location of the optimal parameter set and bars show the range of parameters that produce variations of 1% in the maximum *NS* value. In Figure 6d, we highlight the outliers of general tendencies. (e and f) *NS* values and optimal parameters of JN 3127 and TA4775 in the parameter space of (e) JN3127 and (f) TA4775. GU5324 is not shown due to low model performance.

depicting the range that produces variations of 1% in the optimal value of the *NS* coefficient. Seasonally calibrated *SRF* and *TF* values vary little between sites below 4000 m asl and their values are clustered around 97 mm m$^2$ h$^{-1}$ W$^{-1}$ 10$^{-4}$ and 50 mm h$^{-1}$°C$^{-1}$ 10$^{-4}$, respectively. On the other hand, the intersite variability of these parameters at the locations above 4000 m asl is significantly larger with values of *SRF* between 40 and 75 mm m$^2$ h$^{-1}$ W$^{-1}$ 10$^{-4}$ and values of *TF* between 400 and 2500 mm h$^{-1}$°C$^{-1}$ 10$^{-4}$. In general, large values of *TF* are associated with small values of *SRF*. We detect two outliers in the main trends of the monthly calibrated ETI parameters. These outliers correspond to BE4134 and YE4428 in March 2014 (see Figure 6d) and are caused by a lower than expected SRF optimal value. We think that this low value is connected to the difficulties of the EB model to simulate ablation during late summer 2015 (see Figure 3d–3f). To analyze the issue of equifinality in the ETI model parameters, we present the location of the maximum *NS* value in the ETI parameter space at JN3127 (Figure 6e) and TA4775 (Figure 6f). An equifinality issue is apparent, with a range of parameter sets producing similar values of the *NS* coefficient. Importantly, the performance of the ETI model at JN3127 is not significantly affected by changes in the parameters within the presented ranges (Figure 6e). In contrast, at TA4775, the *NS* values are very sensitive to variations of *SRF*, while variations in *TF* have a small effect (Figure 6f).

Figure 7 shows results from the analysis of transferability of the seasonally calibrated ETI parameters. There is a consistent transferability of ETI parameters among the study sites located within the 3000–4000 m asl elevation band (*NS* between 0.84 and 0.98) and a less consistent one among sites located within the 4000–5000 m asl elevation band (*NS* between 0.63 and 0.89). The ETI parameters optimized for sites above 4000 m asl have a better performance when simulating melt at sites below 4000 m asl (*NS* between 0.71

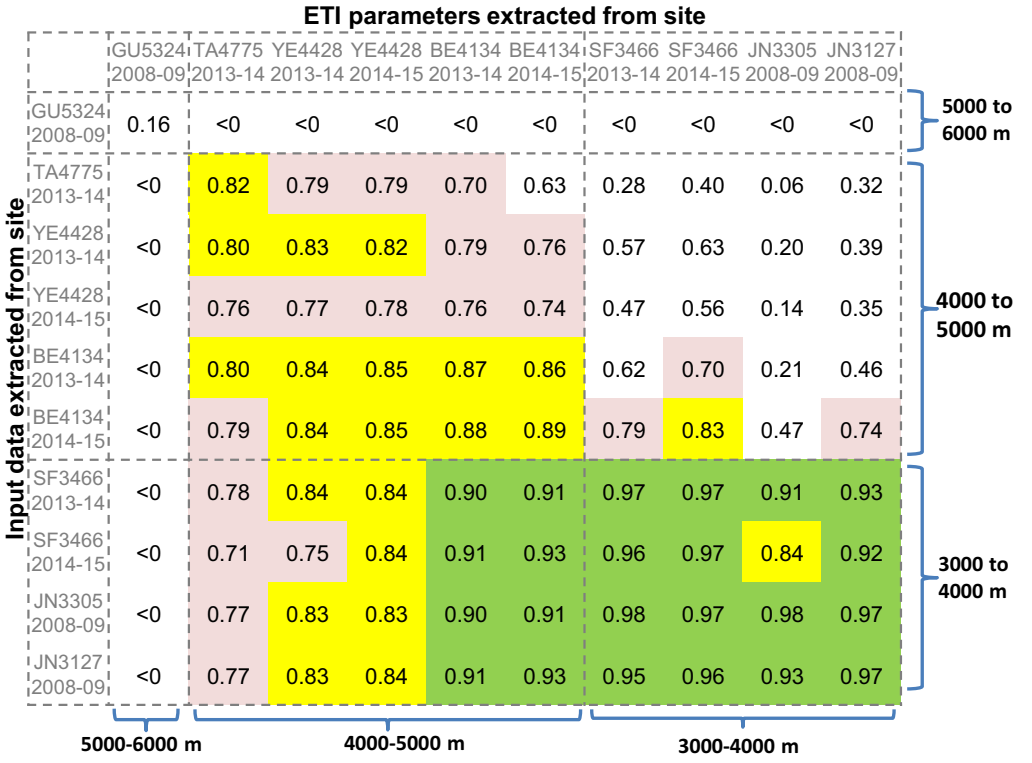


**Figure 7.** *NS* values of the seasonally calibrated ETI model calculated using input data from each site and season (vertical axis) and parameters from the other sites and seasons (horizontal axis). Ranges of *NS* values are shown in green ($\geq$ 0.9), yellow ($\geq$ 0.8 and $<$0.9), and light red ($\geq$ 0.7 and $<$0.8). Blue braces indicate ranges of elevation.

and 0.93) than vice versa (*NS* between 0.06 and 0.83). This behavior can be explained by the fact that at sites below 4000 m asl, there are larger ranges of parameter values producing *NS* coefficients above 0.7, than at sites above this elevation (Figures 6e and 6f). Parameters calculated for GU5324 do not perform well there or at other sites and parameters from other sites do not perform well at GU5324.

#### 4.3.2. Model Performance

Validation metrics for the seasonally and monthly calibrated ETI model are presented in Table 4. The seasonally calibrated ETI model is able to reproduce melt with *NS* values above 0.78 at all sites except for GU5324, where the performance is very poor (*NS* = 0.16). *RMSE* and *MBD* values are low ($<$0.9 and $<$0.12 mm $h^{-1}$, respectively), but the ETI model has a tendency to overestimate melt (all *MBD* values are positive). In general, all validation metrics are considerably better for melt-dominated sites below 4000 m asl than for sites above this elevation. Interestingly, all validation metrics improve when monthly calibrated parameters are used (with the exception of the RMSE at GU5324), especially at sites above 4000 m asl.

In Figure 8, we compare diurnal cycles of surface energy fluxes and melt rates in January 2014 (San Francisco, Bello, Yeso, and Tapado glaciers) and January 2009 (Juncal Norte and Guanaco glaciers). Melt rates from the EB model decrease with elevation in response to lower $S_{net}$ (due to a higher albedo), more negative $L_{net}$, lower $Q_H$, and more negative $Q_L$. An exception to these general trends occurs at TA4775, where the rough penitentes surface produces large turbulent heat fluxes. The performance of the ETI model also decreases with elevation. Most notably, at elevations above 4000 m asl., the ETI model largely overestimates melt during the morning, when air temperatures are warmer than $T_T$, but the surface has not yet reached 0°C. The calibration procedure (based on the maximization of the *NS* value) attempts to reduce the total error by compensating the overestimation produced in the morning by an underestimation of the daily maximum in the afternoon. The validation metrics indicate that, in this midsummer condition (January), the use of monthly calibrated ETI parameters produces improvement in the performance of the ETI model, especially at sites between 4000 and 5000 m asl.

In Figure 9, we analyze the relationship between the performance of the ETI model and the relative importance of mass losses to the atmosphere (the sum of surface sublimation and evaporation) in the total

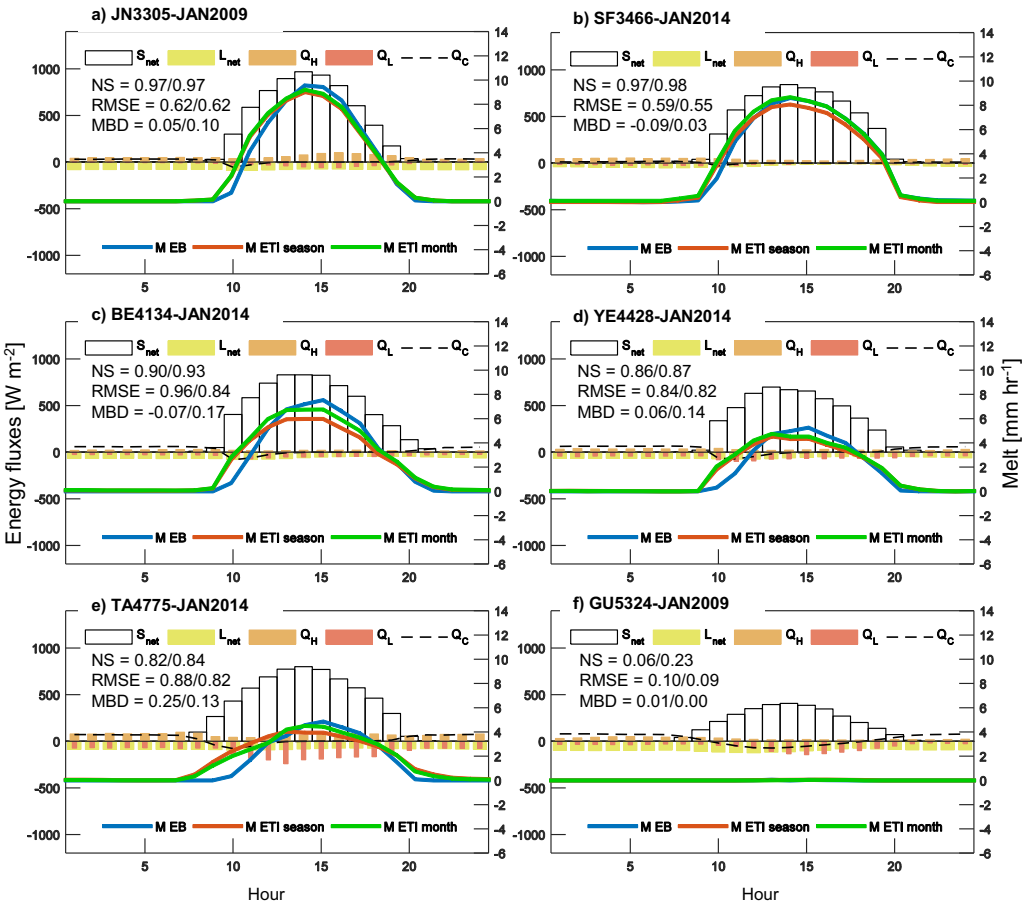


**Figure 8.** Average diurnal cycles of energy fluxes (left axis) and melt rates (right axis) during January 2014 at SF3466, BE4134, YE4428, and TA4775 and during January 2009 at JN3305 and GU5324. Melt rates are calculated using the EB model (M EB), the seasonally calibrated ETI (M ETI season) and the monthly calibrated ETI (M ETI month). At each site, we show *NS*, *RMSE*, and *MBD* values for January of the seasonally (left value) and monthly calibrated (right value) ETI model.

ablation. Mass losses to the atmosphere can be understood as representing the role of $Q_L$ in the energy balance. There is a clear decreasing trend of performance in the seasonally calibrated ETI model as a function of the losses to the atmosphere, which can be seen in the decrease of *NS* (Figure 9a) and the increase of *RMSE* (Figure 9b) and *MBD* (Figure 9c), respectively, for increasing values of the losses to the atmosphere as percentage of total ablation. This behavior is evident also for the *NS* values of the monthly calibrated ETI (Figure 9d), but it is not so clear for the *RMSE* (Figure 9e) or the *MBD* (Figure 9f), which present some small values ($RMSE < 0.6$ mm $h^{-1}$ and $MBD < 0.05$ mm $h^{-1}$) corresponding to large losses to the atmosphere (>10%) at BE4134 and YE4428. These small values of *RMSE* and *MBD* are likely explained by the small magnitude of melt rates.

Results of the evaluation of the ETI model performance are presented in Figure 10. Sites with a higher elevation have a larger percentage of their ETI simulated melt associated with one of the two error types, particularly to error T1 (false positive) (Figure 10a), as suggested by Figure 8. Between 4000 and 5000 m asl, the air temperature threshold approach leads to errors between 4 and 10% of the total simulated melt. At GU5324, these errors reach more than 70%. Figure 10b summarizes results from the correlation analyses between melt from the SEB model and the input variables to the ETI model ($S_{net}$ and $T_a$) at an hourly time step. As we use albedo values measured in the field, we treat $S_{net}$ and not $S_{in}$ as an input variable to the ETI model. While the correlation between melt and $S_{net}$ decreases with elevation, the correlation between melt and $T_a$ varies from site to site without exhibiting a clear trend. Finally, Figure 10c shows the correlation between the temperature-dependent part of the energy inputs ($\Phi$) and meteorological input variables ($T_a$, *RH*, and *WS*). Correlation between $\Phi$ and $T_a$ and *RH* varies from $-0.1$ to 0.75 and does not exhibit a clear relationship

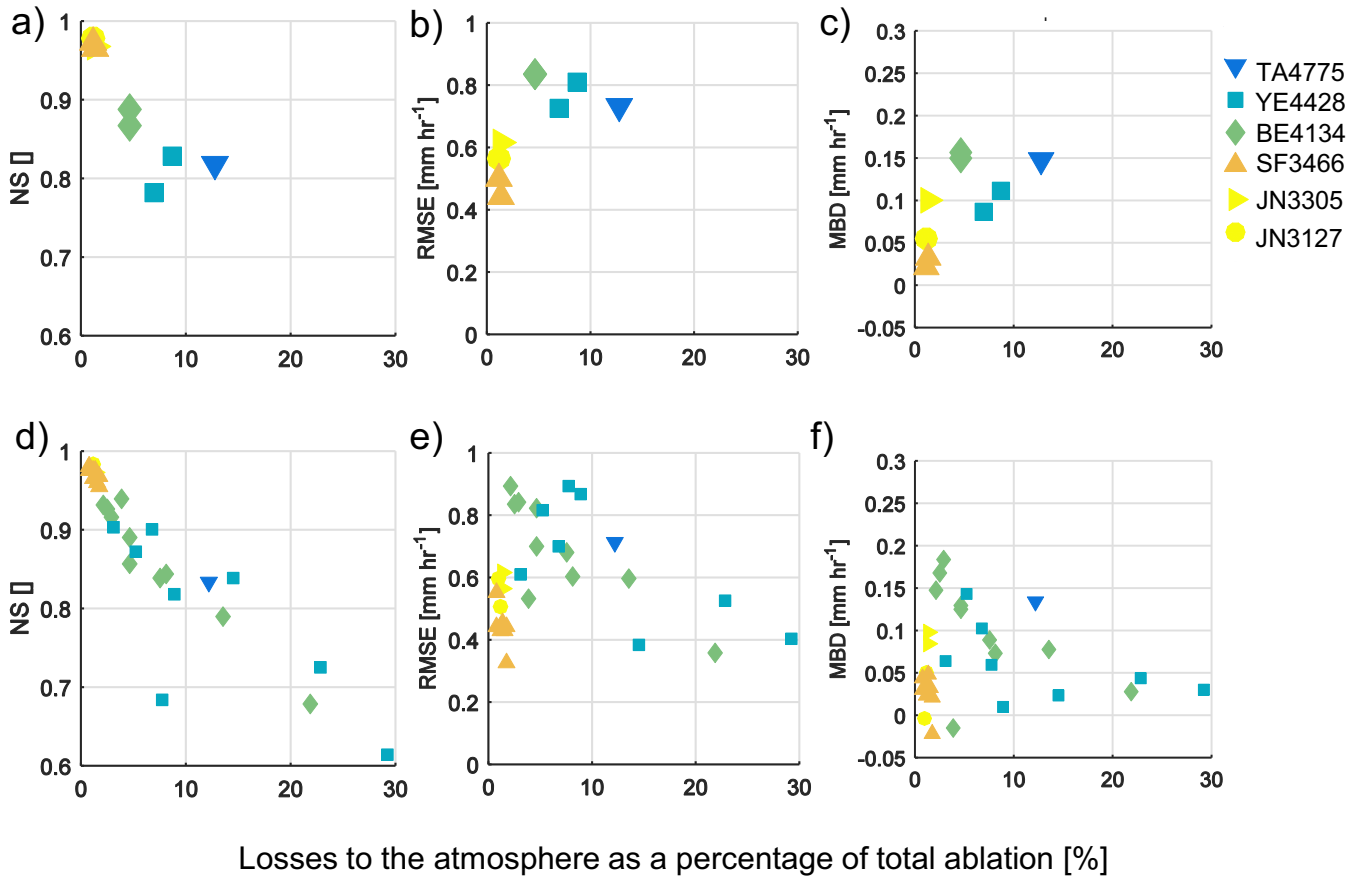


**Figure 9.** *NS*, *RMSE*, and *MBD* values of the ETI model as a function of the losses to the atmosphere (the sum of surface sublimation and evaporation). Losses to the atmosphere are presented as a percentage of total ablation (the sum of surface sublimation, evaporation, and melt). (a–c) Results of seasonally calibrated parameters. (d–f) Results of monthly calibrated parameters. GU5324 is not shown due to the low performance of the ETI model.

with elevation. Interestingly, the correlation between melt and *WS* varies from positive at the lower sites (>0.5 at the sites on Juncal Norte Glacier), to nonsignificant at the sites on San Francisco and Bello glaciers, to negative above 4400 m asl (up to −0.75 at YE4428). These results reflect the fact that at the lower sites, the sum of the turbulent fluxes is dominated by positive values of $Q_H$, which are associated with warm upvalley winds that enhance melt, whereas at the higher sites, turbulent fluxes are dominated by negative values of $Q_L$ that enhance surface sublimation.

## 5. Discussion

### 5.1. Energy and Summer Mass Balance

Our results suggest that the energy balance and ablation across the region, or across a single glacier with a large elevation range, can be roughly described based on altitudinal differences. However, differences in local slope, aspect, wind exposition, and local climate need to be considered when analyzing a new site. From our data set, it is difficult to conclude if, or how, the specific characteristics of each site have biased our results and in which measure. Apart from the interannual differences in our data set, the most evident problems are that our high-elevation sites are also those located in the North-Chile cluster (TA4775 and GU5324), that the highest site is also the windiest (GU5324), and that the lowest sites are also on the only north-facing glacier (Juncal Norte Glacier). However, the energy balance and ablation rates of these sites agree with the altitudinal trends obtained from San Francisco, Bello, and Yeso glaciers, which are likely to be comparable, because they are located in the same region, have similar topographic characteristics and field campaigns were performed during the same seasons.

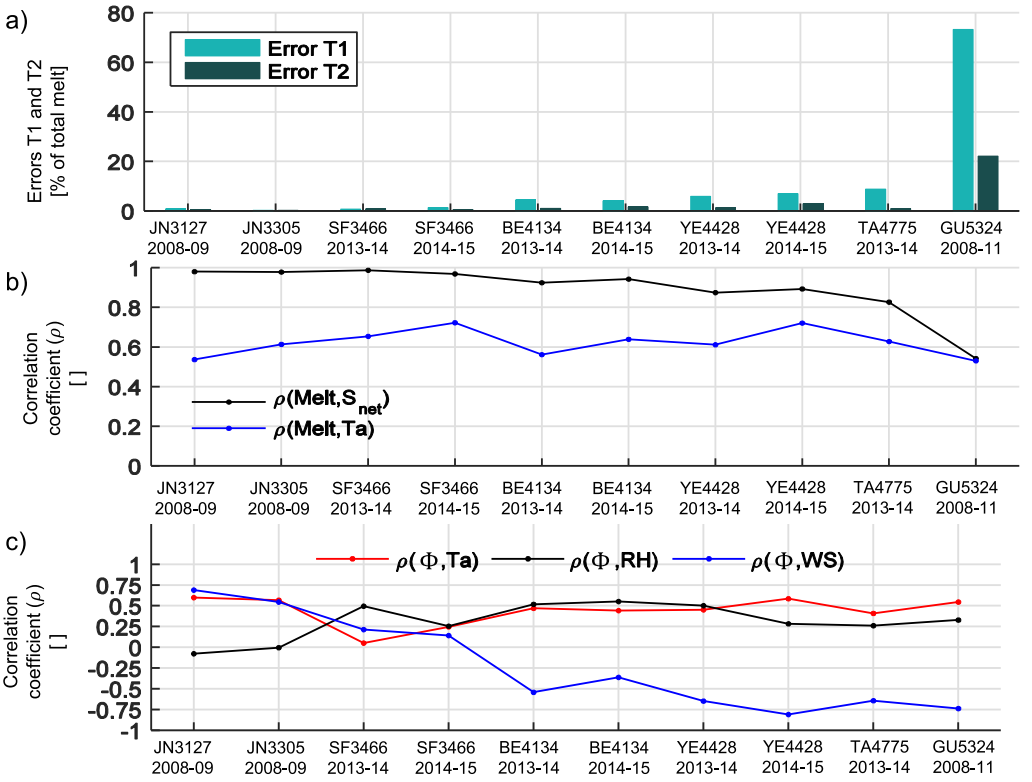


**Figure 10.** (a) Errors produced by the temperature threshold strategy used by the ETI model to identify the onset of melt. Error T1, or false positive, refers to the situation when the EB model does not produce melt, but the ETI model does. Error T2, or false negative refers to the opposite case. Figure 10a refers to total melt simulated by the EB model. (b) Correlation coefficients between melt from the EB model and the input variables to the ETI model ($S_{net}$ and $T_a$) at an hourly time step. (c) Correlation coefficients between the temperature-dependent part of the surface energy balance ($\Phi$) and air temperature ($T_a$), relative humidity ($RH$) and wind speed ($WS$) at an hourly time step.

Based on our results and Figure 5 in particular, we propose a conceptual model that describes the seasonal evolution of summer mass balance along the elevation profile of glaciers in the semiarid Andes (Figure 11). These curves show how, as the ablation season advances, areas where melt is the largest component of ablation spread to higher elevations, refreezing amounts are less important and surface sublimation is likely restricted to high-elevation, wind-exposed sites. Our suggested elevation profiles provide a conceptual base for understanding the summer mass balance of glaciers in the semiarid Andes. These curves are consistent with previous point-scale estimations of ablation rates at different elevations in the semiarid Andes [*Pellicciotti et al.*, 2008; *Favier et al.*, 2009; *Gascoin et al.*, 2011; *MacDonell et al.*, 2013], but are in contrast to results from other regions of the world, such as the inner tropics, where summer is warm and humid, the area below the ELA is extremely small and sublimation rates in summer are low [*Kaser*, 2001; *Sicart et al.*, 2005]. Since total ablation decreases with elevation the importance of surface sublimation in the annual mass balance might be minor on glaciers with a considerable part of their surface area below 4000 m asl. As the mass balance of debris-covered glaciers is controlled by different factors [*Ayala et al.*, 2016], these profiles are likely only valid for debris-free glaciers. A distributed energy balance model applied to multiple glaciers of the region could confirm (or reject) the validity of our summer mass balance conceptualization on each glacier separately or as a regional trend. We note that without data from winter our results are not valid for the annual mass balance.

There are a number of factors that can add uncertainty to results of the EB model in this type of high elevation, remote environment. Extreme meteorological conditions, instrumental errors and tilted sensors frequently affect the data collected for input to the model. In addition, several properties of the snow and ice and physical parameters in the EB model might be subject to large uncertainties in their values, such as the snow density, surface emissivity, and the fraction of $S_{net}$ absorbed by the first layer. As our AWSs were frequently visited and we performed a thorough data quality control, we believe that our field data are of high

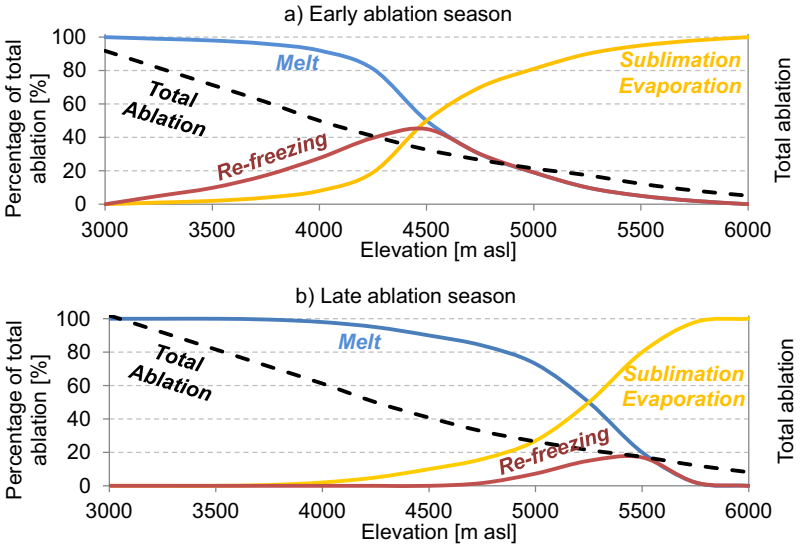


**Figure 11.** Hypothesized elevation profiles of the dominant components of surface ablation on debris-free glaciers of the semiarid Andes of North-Central Chile during the (a) early and (b) late ablation season. Melt, sublimation and refreezing are shown as a percentage of total ablation (left axis) and total ablation is shown in absolute (but hypothetical) values (right axis).

quality and their associated uncertainties are small. Additionally, as suggested by our uncertainty analysis, the general patterns of energy fluxes and total ablation described in the previous sections are not largely affected by the uncertainty in the parameters of the EB model.

Within our set of selected EB model parameters, we find that variations in ablation rates due to parameter uncertainty are mostly correlated to $z_0$ values, which modify the magnitude of the turbulent heat fluxes. We show that the uncertainty in $z_0$ values has a small effect on the altitudinal variations of total ablation, but the exact partitioning of ablation components can be affected by the selection of the $z_0$ value, especially at sites with small ablation rates. In fact, one of the most challenging problems in this type of environment is the selection of a $z_0$ value for areas covered by penitentes [*Nicholson et al*., 2016]. Furthermore, as penitentes develop and the surface roughness increases, some of the assumptions of the EB model hold weaker (uniform ablation, no reflections of shortwave radiation, uniform sky view factor, etc.) and they might be responsible for the failure to simulate surface change during late summer periods (see Figure 2). In this study, we select the $z_0$ value suggested by *Corripio and Purves* [2005] (0.2 m) for penitentes about the same size of the ones we observed at TA4475 and YE4428 (1.5 m). We note that *Corripio and Purves* [2005] estimated this value based on a geometrical approach. Using surface sublimation amounts derived from snow lysimeters, *Wagnon et al*. [1999] estimated lower values of $z_0$ (0.03–0.04 m) for 0.4 m height penitentes on the tropical Andes of Bolivia. Other authors have improved estimations of $z_0$ based on eddy covariance measurements [*Litt et al*., 2015] or geometrical formulae that use high-resolution digital elevation models [*Nicholson et al*., 2016]. Despite the use of a considerably larger $z_0$ value at Tapado and Yeso glaciers, values of $Q_L$ at those sites are not extremely larger than those at the other sites, suggesting that other factors, like wind speed and humidity, largely affect the turbulent fluxes. We also note that the calculation of turbulent fluxes using a bulk-aerodynamic method provides additional uncertainties to EB model results [*Oerlemans and Grisogono*, 2002]. For example, in an analysis of data from Zongo Glacier (Bolivia), *Litt et al*. [2015] showed that this method can underestimate turbulent fluxes compared to results from eddy-covariance methods, and is highly sensitive to surface temperature and the assumed value for $z_0$. Other analyses have concluded that the bulk-aerodynamic method provides acceptable results on sloped glaciers with a katabatic layer [*Denby and Greuell*, 2000].

### 5.2. ETI Model Parameters and Performance

The distribution across sites of the optimal ETI model parameters can be explained by the characteristics of the energy balance at each site. First, the small spread in the optimal ETI parameters observed at sites below 4000 m asl (Figure 6c and 6d) suggest that the overall meteorological and surface conditions are similar at those sites and it explains the good transferability of its parameters (Figure 7). These conditions are low-

albedo surfaces close to melting point, strong radiative forcing and positive values of $Q_H$ that enhance melt, as confirmed by the positive correlation between melt and wind speed shown in Figure 10c. For the same reasons, monthly calibrated and seasonally calibrated ETI parameters have a similar performance below 4000 m asl (Figure 8). Furthermore, as shown in Figure 6e, the large range of ETI parameters that produce a good performance at JN3127 explains why parameters calibrated above 4000 m asl also produce acceptable results when used below this elevation. Second, the large spread in the optimal ETI parameters between 4000 and 5000 m asl is produced when the model attempts to reproduce melt at sites where the surface is below 0°C and the energy inputs are first used to bring the surface to melting point. In those cases, the strong nighttime radiative cooling causes the surface temperature to drop to large negative values. After sunrise, the energy inputs are used first to raise the surface temperature to its melting point and, even though the air temperature is higher than the optimal $T_T$, melt starts a couple of hours later [*Pellicciotti et al*., 2008]. However, once the surface temperature reaches the melting point, the strong $S_{in}$ rapidly produces high values of melt. The fact that the ETI model simulates melt during the early morning, when no melt is observed (error T1 in Figure 10a), leads the optimization procedure to compensate through low *SRF* values. Similarly, in order to reproduce the diurnal maximum melt rate, the optimization procedure results in high *TF* values. Third, the high values of the optimal $T_T$ found at Juncal Norte Glacier (>4°C) have been already reported in the literature and represent the temporal delay of melt onset associated with the removal of the snowpack cold content [*Ragettli and Pellicciotti*, 2012; *Ragettli et al*., 2014]. As explained, at the upper sites there is also a large cold content that needs to be removed before melt starts, but the optimal values of $T_T$ are calibrated to low values. This is because a large value of $T_T$ at the upper sites would ignore a large portion of melt occurring with cold temperatures and strong $S_{in}$. In fact, the low values of $T_T$ found at sites above 4000 m asl, similar to those at the Pyramid station in the Himalaya (5035 m asl) [*Pellicciotti et al*., 2012], reflect the fact that a portion of melt occurs when air temperatures are below 0°C and $S_{net}$ is a large source of energy (Figures 6a and 6b).

As recognized by *Sicart et al*. [2008] and *Hock* [2003], the low performance of the ETI model at high-elevation sites can be explained by the large energy losses from the glacier surface due to radiative cooling and negative values of $Q_L$ associated with surface sublimation. These energy losses strongly increase the cold content of the surface during nighttime, thus undermining the use of an air temperature threshold to identify the onset of melt. Furthermore, the energy inputs from $S_{net}$ are not used directly for melt, and thus, the correlation between melt from the EB model and these energy inputs decreases. A high surface albedo increases this effect by reducing the magnitude of $S_{net}$. In this way, monthly calibrated parameters improve the performance of the ETI model, because the model adapts to the dominant conditions at each month. Interestingly, the correlation between the temperature-dependent part of the energy inputs ($\Phi$) and humidity and air temperature shows no clear relation with elevation. However, the change in the sign of the correlation between this term and wind speed suggests that increasing wind speeds leads to an increase in melt rates on a low-elevation glacier tongue such as that of Juncal Norte Glacier and to a reduction in melt rates at high-elevation sites such as that on Guanaco Glacier. We note that, as we derive albedo values from field radiation data, our results from the EB and ETI models remain a "best-case" scenario in which albedo values are known. If these measurements were not available, the parameterization of surface albedo would play a relevant role for the ETI parameter values of snow-covered sites and might introduce some additional uncertainty. However, the scope of this paper is to establish the limitation and applicability of the ETI model in terms of its model structure and equations, and we therefore use accurate, measured input data to assess its performance to separate uncertainty in the model structure from that in the input data. In addition, as albedo values are less variable for ice than for snow, the ETI parameters of ice-exposed sites are likely not largely affected.

## 6. Conclusions

The unique high-elevation multisite data set analyzed in this study spans a large range of latitude (29°–34°S) and elevation (3127–5324 m asl) and allows a more comprehensive understanding of the energy balance of glaciers in the semiarid Andes than previous studies focusing on a single glacier only. We have also studied the performance of an empirical melt model and have related both the model performance and parameter values to the dominant energy fluxes and the role played by surface sublimation in particular. Our main findings are as follows:

1. Net shortwave and incoming longwave radiations are the largest energy inputs to the glacier surfaces. Net shortwave radiation is mostly controlled by the disappearance of snow through the surface albedo and incoming longwave radiation is controlled by altitudinal differences that affect air temperature and humidity. Turbulent fluxes cancel each other out at the lower sites, but as elevation increases, cold, dry, and wind-exposed conditions increase the magnitude of negative latent heat fluxes, associated with large surface sublimation rates.
2. During the early ablation season, melt dominates glacier ablation at the lower sites, but surface sublimation tends to increase with elevation. At sites where the snowpack has a large cold content, an important part of the available meltwater refreezes. As the ablation season advances, glacier ablation increases in absolute terms, melt increases its relative importance and surface sublimation is only relevant at sites such as those on Tapado and Guanaco glaciers. As the snowpack disappears or increases its temperature, refreezing amounts decrease. In midsummer (January), ablation rates vary from 67.9 mm w.e. $d^{-1}$ at the lowest site (3127 m asl, ~100% corresponding to melt), to 2.3 mm w.e. $d^{-1}$ at the highest site (5324 m asl, >85% corresponding to surface sublimation).
3. At sites below 4000 m asl, where meteorological and surface conditions are favorable to melt, the ETI model has a good performance and its parameters are similar across sites ($SRF \approx 97$ mm $m^2$ $h^{-1}$ $W^{-1}$ $10^{-4}$ and $TF \approx 50$ mm $h^{-1}°C^{-1}$ $10^{-4}$), allowing a transferability in space and time. At sites above 4000 m asl, the ETI model has a lower performance and its parameters have a much larger intersite variability, consistently decreasing the parameter transferability. At the Guanaco Glacier study site (5324 m asl), results of the ETI model are poor, independent of the parameter set. Melt amounts at those elevations are very small and thus the implications of using an ETI model for short-term studies focusing on runoff generation might be minor.
4. At elevations above 4000 m asl, the ability of the ETI model to reproduce melt decreases due to two reasons: (i) the air temperature threshold approach for melt onset does not capture the diurnal variability of melt in cold and strong irradiated environments, and (ii) negative energy fluxes from the radiative cooling and latent heat fluxes associated with surface sublimation decrease the correlation between melt and net shortwave radiation. Monthly calibrated ETI parameters provide better results than simulations with seasonally calibrated parameters.

Building on these findings, we suggest that data collection efforts on these glaciers should be improved and extended to allow for a more reliable estimation of the physical parameters in the energy balance and a better understanding of some poorly understood processes, such as refreezing and sublimation. The incorporation of eddy covariance systems would be useful to improve our understanding of sublimation processes, especially on areas covered by penitentes. In a region with a large latitudinal variation, such as the semiarid Andes, an extension of this type of field campaign to other glaciers in Chile or Argentina would help to better understand ablation patterns and, ultimately, glacier contribution to runoff.

Ablation rates are low where sublimation-favorable conditions dominate. On the long-term, however, they might result in nonnegligible cumulative mass losses on high-elevation glaciers such as Guanaco Glacier, and it seems imperative to prove the magnitude of these long-term mass losses and their importance for runoff generation. As a result, long-term simulations that only use a temperature-index model might need to be extended (to include an estimation of surface sublimation) or adapted (to improve the simulation of melt) to calculate glacier ablation in dry environments. In contrast to melt, which largely depends on the radiation balance, the inclusion of sublimation in a simple parameterization scheme is problematic due to its large dependence on turbulent processes. On the other hand, simulations of melt could be improved by replacing the air temperature threshold parameter for another parameterization that includes a representation of the thermal state of the snow or ice.

**Acknowledgements**

The authors thank all the people from CEAZA, Universidad de Chile, and ETH-Zurich involved in the data collection, especially Sebastián Vivero, Rodrigo Ponce, Cristián Campos, and Alexis Caro. Data from 2013 to 2015 were collected within the project "Modelling the mass balance and water discharges from glaciers of North-Central Chile," funded by DGA, which is kindly acknowledged. Alvaro Ayala acknowledges the *Becas Chile* scholarship program. Shelley MacDonell is supported by CONICYT-FONDECYT 11130484. James McPhee acknowledges CONICYT-FONDECYT 1121184. We thank three anonymous reviewers and the associate editor for their thoughtful comments that helped to improve the manuscript. The data used in this article may be accessed pending an e-mail to shelley.macdonell@ceaza.cl and ayala@ifu.baug.ethz.ch.

## References

Anderson, E. (1976), *A Point Energy and Mass Balance Model of a Snow Cover*, Office of Hydrology, National Weather Service, Silver Spring, Md.

Andreas, E. L. (1987), A theory for the scalar roughness and the scalar transfer coefficients over snow and sea ice, *Boundary Layer Meteorol.*, *38*, 159–184, doi:10.1007/BF00121562.

Arendt, A., et al. (2014), Randolph Glacier Inventory - A Dataset of Global Glacier Outlines: Version 4.0, Global Land Ice Measurements from Space, Digital Media, Boulder Colo.

Ayala, A., F. Pellicciotti, and J. M. Shea (2015), Modeling 2 m air temperatures over mountain glaciers: Exploring the influence of katabatic cooling and external warming, *J. Geophys. Res. Atmos.*, *120*, 3139–3157, doi:10.1002/2013JD021272.

Ayala, A., F. Pellicciotti, S. MacDonell, J. McPhee, S. Vivero, C. Campos, and P. Egli (2016), Modelling the hydrological response of debris-free and debris-covered glaciers to present climatic conditions in the semiarid Andes of central Chile, *Hydrol. Processes*, *30*, 4036–4058, doi:10.1002/hyp.10971.

Azócar, G. F., and A. Brenning (2010), Hydrological and geomorphological significance of rock glaciers in the dry Andes, Chile (27°–33°S), *Permafr. Periglac. Processes*, *21*(1), 42–53, doi:10.1002/ppp.669.

Barnett, T. P., J. C. Adam, and D. P. Lettenmaier (2005), Potential impacts of a warming climate on water availability in snow-dominated regions., *Nature*, *438*(7066), 303–339, doi:10.1038/nature04141.

Bintanja, R., and M. R. van den Broeke (1995), The surface energy balance of antartic snow and blue ice, *J. Appl. Meteorol.*, *34*, 902–926, doi:10.1175/1520-0450(1995)034 < 0902:TSEBOA>2.0.CO;2.

Boisier, J. P., R. Rondanelli, R. D. Garreaud, and F. Muñoz (2016), Anthropogenic and natural contributions to the Southeast Pacific precipitation decline and recent megadrought in central Chile, *Geophys. Res. Lett.*, *43*, 413–421, doi:10.1002/2015GL067265.

Bown, F., A. Rivera, and C. Acuña (2008), Recent glacier variations at the Aconcagua basin, central Chilean Andes, *Ann. Glaciol.*, *48*, 43–48, doi:10.3189/172756408784700572.

Braithwaite, R. (1995), Positive degree-day factors for ablation on the Greenland ice sheet studied by energy-balance modelling, *J. Glaciol.*, *41*(137), 153–160.

Brock, B. W., I. C. Willis, and M. J. Sharp (2006), Measurement and parameterization of aerodynamic roughness length variations at Haut Glacier d ' Arolla, Switzerland, *J. Glaciol.*, *52*(177), 281–297.

Brutsaert, W. (1982), The surface roughness parameterization, in *Evaporation into Atmosphere*, *Theory, History, and Application*, pp. 113–127, Springer, New York, doi:10.1007/978-94-017-1497-6_5.

Carenzo, M. (2012), Distributed modelling of changes in glacier mass balance and runoff, PhD thesis, ETH-Zürich, Zurich, Switzerland.

Carenzo, M., F. Pellicciotti, S. Rimkus, and P. Burlando (2009), Assessing the transferability and robustness of an enhanced temperature-index glacier-melt model, *J. Glaciol.*, *55*(190), 258–274, doi:10.3189/002214309788608804.

Carrasco, J. F., G. Casassa, and J. Quintana (2005), Changes of the 0°C isotherm and the equilibrium line altitude in central Chile during the last quarter of the 20th century, *Hydrol. Sci. J.*, *50*(6), 37–41, doi:10.1623/hysj.2005.50.6.933.

Casassa, G. (1995), Glacier inventory in Chile, *Ann. Glaciol.*, *21*, 2–7.

Cornwell, E., N. P. Molotch, and J. McPhee (2016), Spatio-temporal variability of snow water equivalent in the extra-tropical Andes Cordillera from distributed energy balance modeling and remotely sensed snow cover, *Hydrol. Earth Syst. Sci.*, *20*(1), 411–430, doi:10.5194/hess-20-411-2016.

Corripio, J. (2003), Modelling the energy balance of high altitude glacierised basins in the Central Andes, PhD thesis, Univ. of Edinburgh, Edinburgh, U. K.

Corripio, J., and R. Purves (2005), Surface energy balance of high altitude glaciers in the central Andes: The effect of snow penitentes, in *Climate and Hydrology in Mountain Areas*, edited by C. De Jong, D. Collins, and R. Ranzi, pp. 15–27, John Wiley, Hoboken, N. J.

Corripio, J. G., R. S. Purves, and A. Rivera (2008), Modeling climate-change impacts on mountain glaciers and water resources in *the Central Dry Andes, in Darkening Peaks: Glacier Retreat, Science, and Society*, edited by B. Orlove, E. Wiegandt, and B. H. Luckman, pp. 126–135, University of California Press, Berkeley, Calif.

Dadic, R., R. Mott, M. Lehning, M. Carenzo, B. Anderson, and A. Mackintosh (2012), Sensitivity of turbulent fluxes to wind speed over snow surfaces in different climatic settings, *Adv. Water Resour.*, *55*, 178–189, doi:10.1016/j.advwatres.2012.06.010.

Denby, B., and W. Greuell (2000), The use of bulk and profile methods for determining surface heat fluxes in the presence of glacier winds, *J. Glaciol.*, *46*(154), 445–452, doi:10.3189/172756500781833124.

DGA (2010), Glaciares desde cuencas altiplánicas hasta cuenca del río Petrohué, Inventar. Glaciares, Santiago, Chile. [Available at http://www.dga.cl/productosyservicios/mapas/Paginas/default.aspx, accessed 1 Jun. 2015.]

Ebnet, A., A. G. Fountain, and T. H. Nylen (2005), An index model of stream flow at below freezing-temperatures in Taylor Valley, Antarctica, *Ann. Glaciol.*, *40*, 76–82, doi:10.3189/172756405781813519.

Essery, R., S. Morin, Y. Lejeune, and C. B Ménard (2013), A comparison of 1701 snow models using observations from an alpine site, *Adv. Water Resour.*, *55*, 131–148, doi:10.1016/j.advwatres.2012.07.013.

Falvey, M., and R. Garreaud (2007), Wintertime precipitation episodes in Central Chile: Associated meteorological conditions and orographic influences, *J. Hydrometeorol.*, *8*(2), 171–193, doi:10.1175/JHM562.1.

Favier, V., M. Falvey, A. Rabatel, E. Praderio, and D. Lopez (2009), Interpreting discrepancies between discharge and precipitation in high-altitude area of Chile's Norte Chico region (26–32°S), *Water Resour. Res.*, *45*, W02424, doi:10.1029/2008WR006802.

Finger, D., F. Pellicciotti, M. Konz, S. Rimkus, and P. Burlando (2011), The value of glacier mass balance, satellite snow cover images, and hourly discharge for improving the performance of a physically based distributed hydrological model, *Water Resour. Res.*, *47*, W07519, doi:10.1029/2010WR009824.

Gabbi, J., M. Carenzo, F. Pellicciotti, A. Bauder, and M. Funk (2014), A comparison of empirical and physically based glacier surface melt models for long-term simulations of glacier response, *J. Glaciol.*, *60*(224), 1199–1207, doi:10.3189/2014JoG14J011.

Garreaud, R. D. (2009), The Andes climate and weather, *Adv. Geosci.*, *22*, 3–11, doi:10.5194/adgeo-22-3-2009.

Gascoin, S., C. Kinnard, R. Ponce, S. Lhermitte, S. MacDonell, and A. Rabatel (2011), Glacier contribution to streamflow in two headwaters of the Huasco River, Dry Andes of Chile, *The Cryosphere*, *5*(4), 1099–1113, doi:10.5194/tc-5-1099-2011.

Gascoin, S., S. Lhermitte, C. Kinnard, K. Bortels, and G. E. Liston (2013), Wind effects on snow cover in Pascua-Lama, Dry Andes of Chile, *Adv. Water Resour.*, *55*, 25–39, doi:10.1016/j.advwatres.2012.11.013.

Giesen, R. H., and J. Oerlemans (2012), Calibration of a surface mass balance model for global-scale applications, *The Cryosphere*, *6*(6), 1463–1481, doi:10.5194/tc-6-1463-2012.

Ginot, P., C. Kull, U. Schotterer, M. Schwikowski, and H. W. Gäggeler (2006), Glacier mass balance reconstruction by sublimation induced enrichment of chemical species on Cerro Tapado (Chilean Andes), *Clim. Past*, *2*, 21–30, doi:10.5194/cp-2-21-2006.

Grimm, A. M., V. R. Barros, and M. E. Doyle (2000), Climate variability in southern South America associated with El Niño and La Niña Events, *J. Clim.*, *13*(1), 35–58, doi:10.1175/1520-0442(2000)013 < 0035:CVISSA>2.0.CO;2.

Groot Zwaaftink, C. D., R. Mott, and M. Lehning (2013), Seasonal simulation of drifting snow sublimation in Alpine terrain, *Water Resour. Res.*, *49*, 1581–1590, doi:10.1002/wrcr.20137.

Heynen, M., F. Pellicciotti, and M. Carenzo (2013), Parameter sensitivity of a distributed enhanced temperature-index melt model, *Ann. Glaciol.*, *54*(63), 311–321, doi:10.3189/2013AoG63A537.

Hock, R. (2003), Temperature index melt modelling in mountain areas, *J. Hydrol.*, *282*(1–4), 104–115, doi:10.1016/S0022-1694(03)00257-9.

Hock, R., and B. Holmgren (2005), A distributed surface energy-balance model for complex topography and its application to Storglaciären, Sweden, *J. Glaciol.*, *51*(172), 25–36, doi:10.3189/172756505781829566.

Janke, J. R., A. C. Bellisario, and F. A. Ferrando (2015), Classification of debris-covered glaciers and rock glaciers in the Andes of central Chile, *Geomorphology*, *241*, 98–121, doi:10.1016/j.geomorph.2015.03.034.
Kaser, G. (2001), Glacier climate interaction at low latitudes, *J. Glaciol.*, *47157*, 195–204, doi:10.3189/172756501781832296.
Kaser, G., M. Großhauser, B. Marzeion, and R. G. Barry (2010), Contribution potential of glaciers to water availability in different climate regimes, *Proc. Natl. Acad. Sci. U. S. A.*, *107*(47), 21,300–21,305, doi:10.1073/pnas.1008162107.
Kumar, M., D. Marks, J. Dozier, M. Reba, and A. Winstral (2013), Evaluation of distributed hydrologic impacts of temperature-index and energy-based snow models, *Adv. Water Resour.*, *56*, 77–89, doi:10.1016/j.advwatres.2013.03.006.
Lehning, M., I. Völksch, D. Gustafsson, T. A. Nguyen, M. Stähli, and M. Zappa (2006), ALPINE3D: A detailed model of mountain surface processes and its application to snow hydrology, *Hydrol. Processes*, *2128*, 2111–2128, doi:10.1002/hyp.6204.
Lhermitte, S., J. Abermann, and C. Kinnard (2014), Albedo over rough snow and ice surfaces, *The Cryosphere*, *8*(3), 1069–1086, doi:10.5194/tc-8-1069-2014.
Li, L., and J. W. Pomeroy (1997), Estimates of threshold wind speeds for snow transport using meteorological data, *J. Appl. Meteorol.*, *36*(3), 205–213, doi:10.1175/1520-0450(1997)036 < 0205:EOTWSF>2.0.CO;2.
Liston, G., and M. Sturm (1998), A snow-transport model for complex terrain, *J. Glaciol.*, *44*(148), 498–516, doi:https://doi.org/10.3198/1998JoG44-148-498-516.
Litt, M., J. E. Sicart, and W. Helgason (2015), A study of turbulent fluxes and their measurement errors for different wind regimes over the tropical Zongo Glacier (16°S) during the dry season, *Atmos. Meas. Tech.*, *8*(8), 3229–3250, doi:10.5194/amt-8-3229-2015.
Lliboutry, L. (1954), The origin of penitents, *J. Glaciol.*, *2*(15), 331–338.
Lutz, A. F., W. W. Immerzeel, A. B. Shrestha, and M. F. P. Bierkens (2014), Consistent increase in High Asia's runoff due to increasing glacier melt and precipitation, *Nat. Clim. Change*, *4*(7), 587–592, doi:10.1038/nclimate2237.
MacDonald, M. K., J. W. Pomeroy, and A. Pietroniro (2010), On the importance of sublimation to an alpine snow mass balance in the Canadian Rocky Mountains, *Hydrol. Earth Syst. Sci.*, *14*(7), 1401–1415, doi:10.5194/hess-14-1401-2010.
MacDonell, S., C. Kinnard, T. Mölg, L. Nicholson, and J. Abermann (2013), Meteorological drivers of ablation processes on a cold glacier in the semi-arid Andes of Chile, *The Cryosphere*, *7*(5), 1513–1526, doi:10.5194/tc-7-1513-2013.
MacDougall, A. H., and G. E. Flowers (2011), Spatial and temporal transferability of a distributed energy-balance glacier melt model, *J. Clim.*, *24*(5), 1480–1498, doi:10.1175/2010JCLI3821.1.
Marty, C., R. Philipona, C. Fröhlich, and A. Ohmura (2002), Altitude dependence of surface radiation fluxes and cloud forcing in the alps: Results from the alpine surface radiation budget network, *Theor. Appl. Clim.*, *72*, 137–155.
Masiokas, M., R. Villalba, B. Luckman, C. Le Quesne, and J. Aravena (2006), Snowpack variations in the central Andes of Argentina and Chile, 1951–2005: Large-scale atmospheric influences and implications for water resources in the region, *J. Clim.*, *19*, 6334–6352, doi:https://doi.org/10.1175/JCLI3969.1.
Meza, F. J. (2013), Recent trends and ENSO influence on droughts in Northern Chile: An application of the Standardized Precipitation Evapotranspiration Index, *Weather Clim. Extrem.*, *1*, 51–58, doi:10.1016/j.wace.2013.07.002.
Mölg, T., F. Maussion, W. Yang, and D. Scherer (2012), The footprint of Asian monsoon dynamics in the mass and energy balance of a Tibetan glacier, *The Cryosphere*, *6*(6), 1445–1461, doi:10.5194/tc-6-1445-2012.
Monin, A. S., and A. M. Obukhov (1954), Basic Laws of Turbulent Mixing in the Atmosphere Near the Ground, *Tr. Akad. Nauk SSSR Geoph. Inst.*, *64*, 1963–1987.
Montecinos, A., and P. Aceituno (2003), Seasonality of the ENSO-related rainfall variability in central Chile and associated circulation anomalies, *J. Clim.*, *16*, 281–296, doi:10.1175/1520-0442(2003)016 < 0281:SOTERR>2.0.CO;2.
Nicholson, L., J. Marin, and D. Lopez (2010), Glacier inventory of the upper Huasco valley, Norte Chico, Chile: Glacier characteristics, glacier change and comparison with central Chile, *Ann. Glaciol.*, *50*(53), 111–118.
Nicholson, L. I., M. Petlicki, B. Partan, and S. Macdonell (2016), 3D surface properties of glacier penitentes over an ablation season, measured using a Microsoft Xbox Kinect, *The Cryosphere*, *10*, 1897–1913, doi:10.5194/tc-2015-207.
Niemelä, S., P. Räisänen, and H. Savijärvi (2001), Comparison of surface radiative flux parameterizations: Part I: Longwave radiation, *Atmos. Res.*, *58*, 1–18.
Oerlemans, J., and B. Grisogono (2002), Glacier winds and parameterisation of the related surface heat fluxes, *Tellus Ser. A*, *54*(5), 440–452, doi:https://doi.org/10.3402/tellusa.v54i5.12164.
Ohlanders, N., M. Rodriguez, and J. McPhee (2013), Stable water isotope variation in a Central Andean watershed dominated by glacier and snowmelt, *Hydrol. Earth Syst. Sci.*, *17*(3), 1035–1050, doi:10.5194/hess-17-1035-2013.
Ohmura, A. (2001), Physical basis for the temperature-based melt-index method, *J. Appl. Meteorol.*, *40*(4), 753–761, doi:10.1175/1520-0450(2001)040 < 0753:PBFTTB>2.0.CO;2.
Oyarzún, J., and R. Oyarzún (2011), Sustainable development threats, inter-sector conflicts and environmental policy requirements in the arid, mining rich, northern Chile territory, *Sustain. Dev.*, *274*(December 2009), 263–274.
Pellicciotti, F., B. Brock, U. Strasser, P. Burlando, M. Funk, and J. Corripio (2005), An enhanced temperature-index glacier melt model including the shortwave radiation balance: Development and testing for Haut Glacier d'Arolla, Switzerland, *J. Glaciol.*, *51*(175), 573–587, doi:10.3189/172756505781829124.
Pellicciotti, F., J. Helbing, A. Rivera, V. Favier, J. Corripio, J. Araos, J. E. Sicart, and M. Carenzo (2008), A study of the energy balance and melt regime on Juncal Norte Glacier, semi-arid Andes of central Chile, using melt models of different complexity, *Hydrol. Processes*, *22*, 3980–3997, doi:10.1002/hyp.7085.
Pellicciotti, F., M. Carenzo, J. Helbing, S. Rimkus, and P. Burlando (2009), On the role of subsurface heat conduction in glacier energy-balance modelling, *Ann. Glaciol.*, *50*(50), 16–24, doi:10.3189/172756409787769555.
Pellicciotti, F., C. Buergi, W. W. Immerzeel, M. Konz, and A. B. Shrestha (2012), Challenges and Uncertainties in Hydrological Modeling of Remote Hindu Kush–Karakoram–Himalayan (HKH) Basins: Suggestions for Calibration Strategies, *Mt. Res. Dev.*, *32*(1), 39–50, doi:10.1659/MRD-JOURNAL-D-11-00092.1.
Pellicciotti, F., S. Ragettli, M. Carenzo, and J. McPhee (2014), Changes of glaciers in the Andes of Chile and priorities for future work., *Sci. Total Environ.*, *493C*, 1197–1210, doi:10.1016/j.scitotenv.2013.10.055.
Petersen, L., and F. Pellicciotti (2011), Spatial and temporal variability of air temperature on a melting glacier: Atmospheric controls, extrapolation methods and their effect on melt modeling, Juncal Norte Glacier, Chile, *J. Geophys. Res.*, *116*, D23109, doi:10.1029/2011JD015842.
Pomeroy, J., D. Gray, and P. Landine (1993), The prairie blowing snow model: Characteristics, validation, operation, *J. Hydrol.*, *144*, 165–192.
Prata, A. J. (1996), A new long-wave formula for estimating downward clear-sky radiation at the surface, *Q. J. R. Meteorol. Soc.*, *122*(533), 1127–1151, doi:10.1002/qj.49712253306.

Rabatel, A., H. Castebrunet, V. Favier, L. Nicholson, and C. Kinnard (2011), Glacier changes in the Pascua-Lama region, Chilean Andes (29° S): Recent mass balance and 50 yr surface area variations, *The Cryosphere*, *5*(4), 1029–1041, doi:10.5194/tc-5-1029-2011.

Ragettli, S., and F. Pellicciotti (2012), Calibration of a physically based, spatially distributed hydrological model in a glacierized basin: On the use of knowledge from glaciometeorological processes to constrain model parameters, *Water Resour. Res.*, *48*, W03509, doi:10.1029/2011WR010559.

Ragettli, S., F. Pellicciotti, R. Bordoy, and W. W. Immerzeel (2013), Sources of uncertainty in modeling the glaciohydrological response of a Karakoram watershed to climate change, *Water Resour. Res.*, *49*, 6048–6066, doi:10.1002/wrcr.20450.

Ragettli, S., G. Cortés, J. Mcphee, and F. Pellicciotti (2014), An evaluation of approaches for modelling hydrological processes in high-elevation, glacierized Andean watersheds, *Hydrol. Processes*, *28*(23), 5674–5695, doi:10.1002/hyp.10055.

Ragettli, S., F. Pellicciotti, W. W. Immerzeel, E. Miles, L. Petersen, M. Heynen, J. M. Shea, D. Stumm, S. Joshi, and A. B. Shrestha (2015), Unraveling the hydrology of a Himalayan watershed through integration of high resolution in- situ data and remote sensing with an advanced simulation model, *Adv. Water Resour.*, *78*, 94–111, doi:10.1016/j.advwatres.2015.01.013.

Ragettli, S., W. W. Immerzeel, and F. Pellicciotti (2016), Contrasting climate change impact on river flows from high-altitude catchments in the Himalayan and Andes Mountains, *Proc. Natl. Acad. Sci. U. S. A.*, *113*, 9222–9227, doi:10.1073/pnas.1606526113.

Shea, J. M., W. W. Immerzeel, P. Wagnon, C. Vincent, and S. Bajracharya (2015), Modelling glacier change in the Everest region, Nepal Himalaya, *The Cryosphere*, *9*(3), 1105–1128, doi:10.5194/tc-9-1105-2015.

Sicart, J. E., P. Wagnon, and P. Ribstein (2005), Atmospheric controls of the heat balance of Zongo Glacier (16°S, Bolivia), *J. Geophys. Res.*, *110*, D12106, doi:10.1029/2004JD005732.

Sicart, J. E., R. Hock, and D. Six (2008), Glacier melt, air temperature, and energy balance in different climates: The Bolivian Tropics, the French Alps, and northern Sweden, *J. Geophys. Res.*, *113*, D24113, doi:10.1029/2008JD010406.

Sinclair, K. E., and S. MacDonell (2015), Seasonal evolution of penitente glaciochemistry at Tapado Glacier, Northern Chile, *Hydrol. Processes*, *30*, 176–186, doi:10.1002/hyp.10531.

Strasser, U., M. Bernhardt, M. Weber, G. E. Liston, and W. Mauser (2008), Is snow sublimation important in the alpine water balance?, *The Cryosphere*, *2*, 53–66.

Sturm, M., J. Holmgren, M. König, and K. Morris (1997), The thermal conductivity of seasonal snow, *J. Glaciol.*, *43*(143), 26–41.

Urkidi, L. (2010), A glocal environmental movement against gold mining: Pascua-Lama in Chile, *Ecol. Econ.*, *70*(2), 219–227, doi:10.1016/j.ecolecon.2010.05.004.

Valdés-Pineda, R., J. B. Valdés, H. F. Diaz, and R. Pizarro-Tapia (2015), Analysis of spatio-temporal changes in annual and seasonal precipitation variability in South America-Chile and related ocean-atmosphere circulation patterns, *Int. J. Climatol.*, *1*, 2979–3001, doi:10.1002/joc.4532.

Wagnon, P., P. Ribstein, B. Francou, and B. Pouyaud (1999), Annual cycle of energy balance of Zongo glacier, Cordillera Real, Bolivia, *J. Geophys. Res.*, *104*(D4), 3907–3923.

Wheler, B. A., A. H. Macdougall, G. E. Flowers, E. I. Petersen, H. Paul, and K. E. Kohfeld (2014), Effects of temperature forcing provenance and extrapolation on the performance of an empirical glacier-melt model, *Arct. Antarct. Alp. Res.*, *46*(2), 379–393.

Winkler, M., I. Juen, T. Mölg, P. Wagnon, J. Gómez, and G. Kaser (2009), Measured and modelled sublimation on the tropical Glaciar Artesonraju, Perú, *The Cryosphere*, *3*(1), 21–30, doi:10.5194/tc-3-21-2009.